UNIVERSITAT POLITÈCNICA DE CATALUNYA
BARCELONATECH
Escola d'Enginyeria de Barcelona Est

FINAL DEGREE PROJECT

Degree in Chemical Engineering

MODELLING OF THE MOBILITY OF NANOPARTICLES IN POROUS MEDIA APPLIED TO GROUNDWATER REMEDIATION

REPORT – ECONOMIC ANALYSIS

Author: Estel – Lara Coloma Gonzalez
Supervisor: Vicenç Martí Gregorio

Call: May 2018

Resum

Actualment les anomenades nanopartícules (NPs), ja siguin tant d'origen natural com antropogènic, són àmpliament presents en el subsòl. En molts casos poden ser de caràcter tòxic o es poden introduir deliberadament per eliminar contaminants, degut a la seva gran àrea superficial i càrrega elèctrica. És per aquest motiu que la seva importància ha crescut en els últims anys i, per tant, el seu estudi. Així doncs, s'ha començat a estudiar recentment com aprofitar l'alta reactivitat de les solucions de NPs per tal de tractar les aigües subterrànies contaminades.

Entendre els mecanismes que controlen el transport de les NPs en forma de dissolució col·loïdal aquosa en ambients subterranis és de crucial importància en els temps actual. És per aquest motiu que en el present treball s'exposen de manera entenedora les equacions que regeixen la mobilitat en medis porosos de les NPs i el seu comportament al modificar les variables més importants que s'explicaran a continuació. A més a més es presenten i s'exemplifiquen els fenòmens majoritaris de deposició i transport basant-ho en referencies bibliogràfiques fiables.

En la part final del projecte es modela un cas amb dades reals d'un experiment que s'està duent a terme actualment a la República Txeca, per tal d'aplicar els coneixements obtinguts amb anterioritat i extreure les corresponents conclusions sobre els mecanismes que actuen.

Resumen

Actualmente las llamadas nanopartículas (NPs), ya sean tanto de origen natural como antropogénico, están ampliamente presentes en el subsuelo. En muchos casos pueden ser de carácter tóxico o se pueden introducir deliberadamente para eliminar contaminantes, debido a su gran área superficial y carga. Es por este motivo que su importancia ha crecido en los últimos años y, por tanto, su estudio. Así pues, se ha empezado a estudiar recientemente como aprovechar la alta reactividad de las soluciones de NPs para tratar las aguas subterráneas contaminadas.

Entender los mecanismos que controlan el transporte de las NPs en forma de disolución coloidal acuosa en ambientes subterráneos es de crucial importancia en los tiempos actuales. Es por este motivo que en el presente trabajo se exponen de manera comprensible las ecuaciones que rigen la movilidad en medios porosos de las NPs y su comportamiento al modificar las variables más importantes que se explicarán a continuación. Se presentan y se ejemplifican los fenómenos mayoritarios de deposición y transporte basándolo en referencias bibliográficas fiables.

En la parte final del proyecto se modela un caso real con los datos de un experimento que actualmente se está llevando a cabo en la República Checa, para aplicar los conocimientos adquiridos con anterioridad y extraer las conclusiones correspondientes sobre los mecanismos que actúan.

Abstract

Nowadays, the nanoparticles (NPs), both of natural and anthropogenic origin, are widely present in the subsoil. In many cases, they can be toxic or deliberately introduced to remove pollutants, due to their large surface area and charge. It is for this reason that its importance has grown in the recent years and, therefore, its study. Consequently, recent research has begun on how to take advantage of the high reactivity of NP solutions to treat polluted groundwater.

Understanding the mechanisms that control the transport of NPs in the form of aqueous colloidal dissolution in groundwater is a matter of crucial importance nowadays. For this reason, in the present work, the equations governing mobility in porous media of NPs and their behavior are defined in an understandable way. Moreover, it is explained how modifying the most important variables affects the mobility. The main deposition and transport phenomenon are illustrated and exemplified based on reliable bibliographical references.

In the final part of the project a migration test is modeled with current data from an experiment that is being carried out in Czech Republic, in order to apply the knowledge acquired previously and draw the corresponding conclusions about the mechanisms occurring in the experiment.

Acknowledgments

To my parents, Neus and Joan, for the unconditional backing during all this months and to always believe in me.

To my project director, Vicenç Martí, for the guidance and patience through the development of this end-of-degree thesis.

And to Melani, and our mutual support during the most crucial days.

Symbols

Symbol	*Name*	*Units*
A_{rip}	Ripening coefficient	-
C_{in}	Injection concentration	[M L^{-3}]
C_0	Initial concentration	[M L^{-3}]
c	Colloid concentration in the liquid phase	[M L^{-3}]
D	Hydrodynamic dispersion coefficient	[L^2 T^{-1}]
d_{50}	Median porous medium grain diameter	[L]
d_p	Particle diameter	[L]
IS	Ionic strength	[M L^{-3}]
k_{att}	Attachment coefficient	[T^{-1}]
k_{det}	Detachment coefficient	[T^{-1}]
k_{eq}	Equilibrium constant	[-]
L	Column length	[L]
m	Mass of nanoparticles	[M]
n	Porosity of the packed bed	-
Q	Discharge rate	[L^3 T^{-1}]
q	Darcyan velocity	[L T^{-1}]
R_{eq}	Theoretical retardation factor	[-]
R_{exp}	Experimental retardation factor	[-]
r	Radius of the column	[L]
s	Colloid concentration in the solid phase	[-]

s_{max}	Maximum solid phase concentration of attached colloids	[-]
t	Time	[T]
t_{50}	Time at the 50% of the total concentration	[T]
t_{inj}	Injection time	[T]
V	Total volume	[L^3]
v	Pore water velocity	[$L\ T^{-1}$]
v_{NP}	Particle velocity	[$L\ T^{-1}$]
v_{tracer}	Tracer velocity	[$L\ T^{-1}$]
x	Distance that the particles travel from the inlet point	[L]
α	Colloid sticking efficiency or attachment efficiency	-
α_L	Longitudinal dispersivity	[L]
β_{rip}	Ripening exponent	-
β_{str}	Straining fitting parameter	-
Δ_t	Increase of time	[T]
η	Single collector removal efficiency	-
η_0	Single collector removal efficiency	-
ρ	Dissolution density	[$M\ L^{-3}$]
ρ_b	Bulk density of the solid matrix	[$M\ L^{-3}$]
ρ_p	Particle density	[$M\ L^{-3}$]
ρ_s	Grain density	[$M\ L^{-3}$]

CONTENTS

RESUM I

RESUMEN II

ABSTRACT III

ACKNOWLEDGMENTS IV

SYMBOLS V

CONTENTS VII

LIST OF TABLES IX

LIST OF FIGURES 1

1 INTRODUCTION 3

1.1 Objectives 5

2 APPLICATION OF NANOPARTICLES FOR GROUNDWATER REMEDIATION 7

2.1 The problem of groundwater contamination 8

2.2 Techniques of groundwater remediation 8

2.3 Steps for the application of NPs in groundwater 11

3 PARTICLE TRANSPORT IN POROUS MEDIA 12

3.1 Mechanisms controlling particle transport 12

3.1.1 Clean bed filtration 14

3.1.2 Linear 15

3.1.3 Blocking 15

3.1.4 Ripening 16

3.1.5 Straining and filtration 17

3.2 Factors that influence the NPs transport 19

3.2.1 Sand-particle interactions 19

3.2.2 Ionic strength 21

3.2.3 Fluid viscosity 22

3.2.4 Flow velocity 22

4 SIMULATIONS OF THE CASE STUDIES 23

4.1 Modelling with MNMs 2018 23

4.1.1 Pore volume 25

4.1.2 Bulk and grain density 25

4.1.3 Retardation factor 25
4.1.4 Pore velocity 26
4.1.5 Total concentration 26
4.2 Linear case study 27
4.3 Blocking case study 31
4.4 Ripening case study 36
4.5 Straining case study 42
5 MODELLING A MIGRATION TEST 49
5.1 Experimental setup 49
5.2 Characteristics of the used nanoparticles 50
5.3 Experimental data 53
5.4 Modelling NA84 with MNMs 58
5.4.1 Ripening simulations 60
5.4.2 Straining simulations 62
6 ENVIRONMENTAL IMPACT 65
7 CONCLUSIONS 66
8 ECONOMIC ANALYSIS 67
8.1 Time programming 67
8.2 Costs of the project 67
8.2.1 Software resources 68
8.2.2 Material resources 68
8.2.3 Personnel costs 68
8.2.4 Total budget 69
9 REFERENCES 70

List of tables

Table 1. Properties for the simulation of the linear mechanism (Source: Tosco and Sethi, 2009). 27
Table 2. Stress period time for linear simulation. 28
Table 3. Properties for the simulation of the blocking mechanism (Source: Tosco et al., 2016a). 32
Table 4. Stress period time for blocking simulation. 32
Table 5. Properties for the simulation of the ripening mechanism (Source: Hosseini and Tosco, 2013). 36
Table 6. Stress period time for ripening simulation. 37
Table 7. Properties for the simulation of the straining mechanism (Source: Torkzaban et al., 2008). 43
Table 8. Stress period time for straining simulation. 44
Table 9. Characteristics of the NPs (Source: Ribas, 2017). 52
Table 10. Retardation factor for all the case studies. 57
Table 11. Properties for the simulation of the experiment for NA84 (Source: Černík, 2018). 58
Table 12. Properties for the ripening site for NA84. 59
Table 13. Properties for the ripening site for NA84. 59
Table 14. Stress period time for NA84 simulation. 59
Table 15. Software costs. 68
Table 16. Material costs. 68
Table 17. Total direct costs. 69
Table 18. Total cost for the project. 69

List of figures

Figure 1. Example of pump-and-treat system with two extraction wells (Source: EPA, 2012). 9
Figure 2. Permeable reactive barrier mechanism (Source: OST-FOUNDED TECHNOLOGIES). 9
Figure 3. In situ technologies used to treat polluted groundwater and soils (Source: Muller and Nowack, 2010). 10
Figure 4. Classification of the colloid deposition mechanisms according to the type of interaction (Source: Own elaboration). 13
Figure 5. Clean bed filtration pore scale particle retention (Source: Tosco et al., 2014). 14
Figure 6. Linear pore scale particle retention (Source: adapted from Tosco et al., 2014). 15
Figure 7. Blocking pore scale particle retention (Source: Tosco et al., 2014). 15
Figure 8. Ripening pore scale particle retention (Source: Tosco et al., 2014). 16
Figure 9. Straining pore scale particle transport (Source: Tosco et al., 2014). 17
Figure 10. Illustration of strained colloids in the smallest regions of the soil pore space (Source: Bradford et al., 2006). 17
Figure 11. Particle deposition mechanisms (Source: Tosco et al., 2013). 20
Figure 12. Particle removal efficiency in a granular filter (Source: Messina et al., 2015). 20
Figure 13. Values of attachment term (left), detachment term (right) as a function of ionic strength in logarithmic scale (Source: adapted from Tosco et al., 2013). 21
Figure 14. Simulated breakthrough curve for colloid transport in linear site. 28
Figure 15. Simulated breakthrough curve in MNM1D (Source: Tosco and Sethi, 2009). 28
Figure 16. Profile of colloid concentration onto solid phase vs the distance along the column in linear site. 29
Figure 17. Profile of colloid concentration onto liquid phase vs the distance along the column in linear site. 30
Figure 18. Profile of total colloid concentration vs distance along the column in linear site. 30
Figure 19. Liquid ratio vs distance along the column in linear site for four chosen times. 31
Figure 20. Simulated breakthrough curve for colloid transport in blocking site. 33
Figure 21. Simulated breakthrough curve for SLGO nanoparticles using MNMs (Source: adapted from Tosco et al., 2016a). 33
Figure 22. Profile of colloid concentration onto solid phase vs the distance along the column in blocking site. 34
Figure 23. Profile of colloid concentration onto liquid phase vs the distance along the column in blocking site. 35
Figure 24. Profile of colloid concentration in solid and liquid phase vs distance along the column in blocking site. 35
Figure 25. Simulated breakthrough curve for colloid transport in ripening site. 38
Figure 26. Simulated breakthrough curve for nZVI particles (Source: adapted from Hosseini and Tosco, 2013). 38
Figure 27. Simulated breakthrough curve for NaCl tracer in ripening site. 39
Figure 28. Simulated breakthrough curve for NaCl tracer (Source: adapted from Hosseini and Tosco, 2013). 40
Figure 29. Profile of colloid concentration onto solid phase vs the distance along the column in ripening site. 40

Figure 30. Profile of colloid concentration onto liquid phase vs the distance along the column in ripening site. 41
Figure 31. Profile of colloid concentration in solid and liquid phase vs distance along the column in ripening site. 41
Figure 32. Liquid ratio vs distance along the column in linear site for four chosen times. 42
Figure 33. Simulated breakthrough curve for colloid transport in ripening site. 45
Figure 34. Simulated breakthrough curve for CML colloids in MIX sand, with HYDRUS – 1D code (Source: Torkzaban et al., 2008). 45
Figure 35. Profile of colloid concentration onto solid phase vs the distance along the column in straining site. 46
Figure 36. Profile of colloid concentration onto liquid phase vs the distance along the column in straining site. 47
Figure 37. Profile of colloid concentration in solid and liquid phase vs distance along the column in straining site. 47
Figure 38. Liquid ratio vs distance along the column in straining site for four chosen times. 48
Figure 39. Experimental setup for transport tests (Source: own elaboration). 49
Figure 40. SEM images of the particles: NA64 (a), NA84 (b), 25P (c), STAR 197 (d) and A01 (e) (Source: Ribas, 2017). 51
Figure 41. Granulometric distribution obtained by laser diffraction of commercial and used NPs (Source: Ribas, 2017). 51
Figure 42. Profile of magnetic susceptibility versus the distance for NA64 particles (Source: Černík, 2018). 54
Figure 43. Profile of magnetic susceptibility versus the distance for NA84 particles (Source: Černík, 2018). 54
Figure 44. Profile of magnetic susceptibility versus time at the outlet of the column for NA 64 particles. 55
Figure 45. Profile of magnetic susceptibility versus time at the outlet of the column for NA 84 particles. 56
Figure 46. Signal ratio versus time for NA84 particles. 56
Figure 47. Simulated breakthrough curve for NA84 in ripening site. 60
Figure 48. Profile of colloid concentration onto solid phase vs the distance along the column in ripening site for NA84. 60
Figure 49. Profile of colloid concentration onto liquid phase vs the distance along the column in ripening site for NA84. 61
Figure 50. Profile of colloid concentration in solid and liquid phase vs distance along the column in ripening site for NA84. 61
Figure 51. Simulated breakthrough curve for NA84 in straining site. 62
Figure 52. Profile of colloid concentration onto solid phase vs the distance along the column in straining site for NA84. 63
Figure 53. Profile of colloid concentration onto liquid phase vs the distance along the column in straining site for NA84. 63
Figure 54. Profile of colloid concentration in solid and liquid phase vs distance along the column in straining site for NA84. 64
Figure 55. Gantt diagram for the present project. 67

1 Introduction

Particle transport and deposition in porous media are important processes occurring in natural and engineered systems. One application involving particle transport and deposition is the design of remediation techniques by using nanoparticles as reagents.

Understanding the mechanisms that control the transport and fate of colloidal particles in subsurface environments is a crucial issue faced by several researchers in the last years. In many cases, natural colloids have been shown to play a major role in the spreading of contaminants, while manufactured micro-and nanoparticles, which are nowadays widely spread in the subsurface, can be toxic themselves. On the other hand, it has been also studied the use of highly reactive micro- and nanoparticle suspensions for the remediation of contaminated aquifers.

Due to the importance of filtration theory for describing environmental engineering processes, the main purpose of the present project is to clarify several aspects about the equations that govern the nanoparticles (NPs) transport and ensure that the main mechanisms of mobility in porous media can be simulated with the software MNMs 2018. This software, developed for quantitative analysis of laboratory-scale column tests and NPs injections in simplified geometries, is a useful tool for the preliminary optimisation of pilot injections in the framework of a nanoremediation design. An innovative environmental nanotechnology aimed at reclaiming contaminated aquifers.

The simulation method represents an advancement for the control of nanomaterial fate in the environment, and can enhance nanoremediation making it an effective alternative compared to conventional techniques of decontamination.

1.1 Objectives

The main objectives of this work will be to acquire a greater knowledge about the phenomena that govern the transport of nanoparticles in groundwater and understanding the phenomena at laboratory scale from reliable references. To achieve this aim, several simulations are carried out with the one-dimensional mathematical model MNMs 2018, developed by a team of researchers from the Università di Torino. This program is a tool that allows modelling the transport of micro and nanoparticles in porous media.

Furthermore, for a better understanding of the role of the nanoparticles used for the remediation of aquifers, a simulation of a real nowadays column experiment is performed and, afterwards, analysed in order to apply the knowledge acquired in the previous chapters.

2 Application of nanoparticles for groundwater remediation

The rapid growth of nanotechnology is giving rise to mass production and widespread application of nanoparticles (NPs). During their production, application, and disposal, the NPs inevitably enter the environment. Because of their potential toxicity as well as their role as carriers of contaminants, the release of NPs may lead to environmental contamination (WANG ET AL., 2012).

However, some engineered NPs are thought as remediation agents when injected at contaminated sites, mainly groundwater. Colloidal suspensions consist in finely divided NPs dispersed in a continuous medium. In the present context, the dispersed phase is a solid and the continuous phase is a dissolution that will be finally replaced by groundwater. Understanding and modelling the transport and the deposition of colloidal particles in saturated porous media (groundwater) is therefore a key aspect both in the short-term (design of a field-scale injection) and the long-term (spreading in the environment) prediction of particle distribution. The mobility of nanoparticles in saturated porous media is determined by the combination of particle-particle and particle-porous medium physico-chemical interactions, which typically result in dynamic deposition and release phenomena (KRETZSCHMAR ET AL., 1999).

There are several challenges for designing remediation strategies and selecting appropriate approaches, including complex geo-physical-chemical conditions, contaminant mixtures and economic considerations (ZHANG ET AL., 2017).

The terms colloid and nanoparticle are not strictly interchangeable but could match in some context. A colloid is a mixture which has solid particles dispersed in a liquid medium. This term applies only with the critical size range (or particle diameter) typically ranging from nm to µm. On contrast, NPs are particles between 1 and 100 nm in size with a surrounding interfacial layer. Colloids can contain particles too large to be nanoparticles, and nanoparticles can exist in non-colloidal form, for examples as a powder or in a solid matrix (TOSCO AND SETHI, 2009). As this study will be focused on dissolutions and solids that are NPs with a size from nm to some micrometres, colloids and nanoparticles will be used as a synonymous.

2.1 The problem of groundwater contamination

Groundwater is by far the most abundant and readily available source of freshwater followed by lakes, reservoirs, rivers and wetlands. Soil and groundwater contamination are closely linked. Methods targeting soil contamination indirectly affect the quality of the groundwater, and vice versa (Mueller and Nowack, 2010).

Contamination that affects groundwater is usually produced by infiltration through the ground, which usually requires an analysis of the soil-groundwater system, to determine pollution mechanisms and alternatives to remediation. In particular, there are three fundamental factors to consider when analysing the remediation alternatives: the focus of contamination, the infiltration mechanism, and the type of contaminant (Fornés, 2003).

The effects of groundwater pollution are wide. Human infectious disease is one of the more serious effects of water pollution especially in rural countries that are still developing and where sanitation is rarely present. This alone could cause hundreds of thousands of health problems in the area contaminated. An average 7 million people are sickened in the US from drinking polluted water yearly. Contamination of ground water can result in poor drinking water quality, loss of water supply, degraded surface water systems, high clean-up costs, high costs for alternative water supplies and/or potential health problems (Pawari and Gawande, 2015).

2.2 Techniques of groundwater remediation

Conventional remediation technologies for groundwater and soil include ex-situ methods (e.g. soil washing), on-site methods (e.g. pump-and-treat) and in-situ methods (e.g. permeable reactive barriers) (Zhao et al., 2016). Soil and groundwater remediation is generally very expensive, and conventional methods are not always successful or they take a long time for the remediation to become effective.

One conventional on-site technique is pump-and-treat, this involve pumping contaminated water to the surface for treatment, Figure 1 represents in schematic and simplified way the technique used for it. The treatment system may consist of a single clean-up method, such as activated carbon or air stripping, to clean the water (EPA, 2012). However, the complete aquifer restoration is an unrealistic goal for many, if not most, contaminated sites. Furthermore, this technique would take a very long time (50 – 100 years) to meet clean-up goals (EPA, 1996).

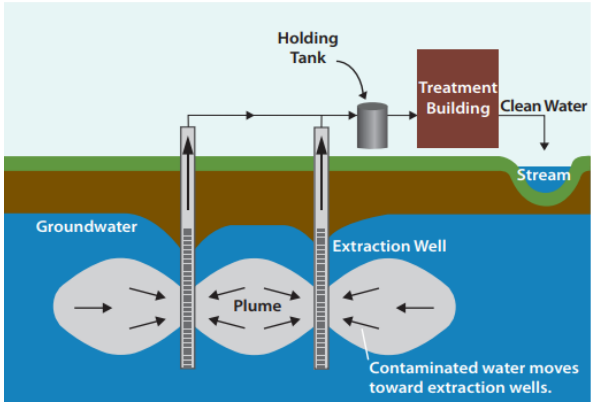

Figure 1. Example of pump-and-treat system with two extraction wells (Source: EPA, 2012).

Compared to ex-situ and on-site remediation practices (were soil or groundwater is extracted and transported) the in-situ technology holds the potential to be not only much less environmentally destructive, but also cost-effective (KARN ET AL., 2009). In addition, in-situ techniques can reach contaminants that are not reachable with other conventional technologies, such as contaminants located in deep acquirers or those underneath surface barriers, where in-situ techniques may be the only possible solution (ZHAO ET AL., 2016).

An example for a conventional in-situ technique is the permeable reactive barriers (PRBs) and the mechanism is relatively simple: a permeable, subsurface barrier containing a reactive material (such as granular iron) is constructed across the path of a contaminant plume as illustrated in Figure 2. When groundwater passes through the reactive barrier, contaminants are either immobilized or chemically transformed to a more desirable state (OST-FOUNDED TECHNOLOGIES).

However, they have some important limitations. Technical difficulties and associated costs of excavation restrict the depth of the barrier to 30 - 40 m. Moreover, it can only address contaminant plumes that flow through the barrier and hence they do not contribute to the active removal of the source. This has a direct impact on the duration of the remediation and the availability of the land for resale or reuse (MUELLER ET AL., 2012).

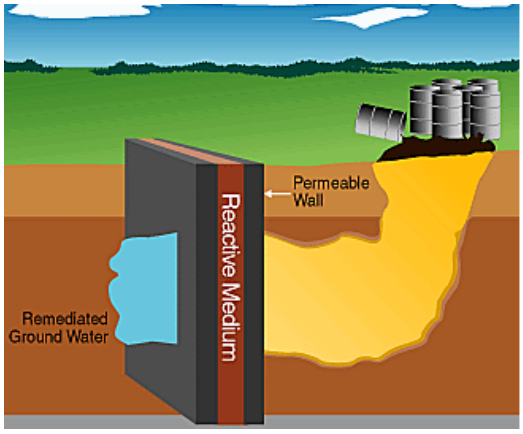

Figure 2. Permeable reactive barrier mechanism (Source: OST-FOUNDED TECHNOLOGIES).

For in-situ treatment, it is necessary to create a reactive zone around where the contamination is, and the use of suspensions of nanoparticles (NPs) allow this objective.

The most important benefits of NPs are consequence of their small size, normally in the theoretical range of 1–100 nm that could be extended to 1 µm. The reduction of the size increases the specific external surface; this improves the chemical reactivity of NPs compared with higher sizes. Moreover, the nano-scale size increase the percentage of atoms exposed to surface and this maximize the optical, electrical and magnetic properties.

For the specific application in groundwater remediation, NPs should have the following requirements: large reactivity, high stability and to have easily controllable mobility. Furthermore, it is important to understand the environmental risk-benefit balance for the use of nanoparticles (explained in detail in chapter 6. Environmental impact)

There are different mechanisms to remediate with NPs. For groundwater can be the in-situ injection of NPs to form a reactive zone (1) or directly act on a Dense Non-Aqueous Phase Liquid (DNAPL) (2) , as shown in Figure 3. For topsoil remediation it is needed an incorporation of NPs into the contaminated soil to adsorb or degrade pollutants (3).

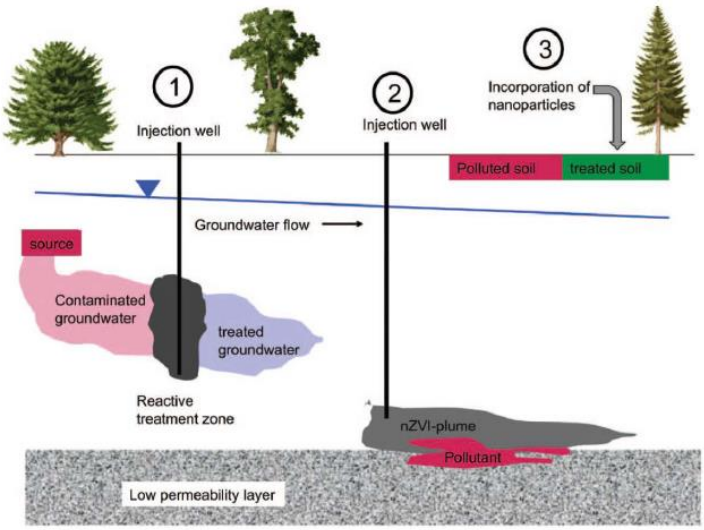

Figure 3. In situ technologies used to treat polluted groundwater and soils (Source: Muller and Nowack, 2010).

The first alternative in Figure 3 is the most used and tries to improve the permeable reactive barriers conventional technique using NPs. For applications in topsoil (third alternative in Figure 3), nanoparticles can be worked into the surface of the contaminated soil using conventional agricultural practices and thus is not an in-situ, but an on-site method.

The use of injected NPs suspensions opens and important field of application that have been extensively demonstrated in EU projects such as NANOREM (NANOREM, 2017).

2.3 Steps for the application of NPs in groundwater

Three steps are used to implement a remediation with NPs in groundwater:

1. **Laboratory methods.** In this step, groundwater is sampled from the site and brought to a laboratory. The sample is analysed with standard laboratory methods to known the amount of contaminants and several reactivity batch test could be performed to know the type and concentration of NPs need for remediation.

   The stability of NPs suspension is also a key point and some sedimentation test and measurement of parameters such as zeta-potential could be performed. As a result, maybe some dispersant additives have to be added to maintain the NPs in suspension. The suspensions of NPs have to be tested in terms of mobility. A column test could be performed with standard porous media (sand) or material from aquifer in order to see the radius of influence of NPs.
2. **Pilot tests.** In this step a test in a small part of the contaminated site could be performed. Normally there is available an injection well and several control wells around to test a real injection of NPs and see if they work in the field. In the control wells samples are analysed periodically to see the elimination of contaminants. In this step several m^3 of NPs suspension are injected.
3. **Full-scale application.** After a successful pilot test, the remediation with NPs could be applied to the entire site.

From these three steps, the effort of the present work will be put in step 1, specifically in the column mobility test.

3 Particle transport in porous media

3.1 Mechanisms controlling particle transport

In this section a review of the phenomena occurred in the transport of nanoparticles will be done. Thereafter, the mechanisms explained will be simulated in MNMs program.

Accurate knowledge of the processes that control the transport and deposition of colloids in subsurface environments is needed to clean water resources from a wide variety of contaminants.

The behaviour of the NPs can be describes with the help of some simplified equations and mathematic models as shown below. The mechanisms controlling NP transport are the same regardless of the geometry (1D, radial or 3D) and the scale. Consequently, they can be determined on smaller scales (namely columns) and then can be applied to larger scales (radial or full 3D). Parameters calibrated by using the 1D model for laboratory column tests are directly transferable to the 3D model (NANOREM, 2017).

NPs are dispersed, transported and deposited within groundwater. Thus, they are subject to processes like filtration, straining, physical-chemical deposition and aggregation, as they are attracted to the surfaces of the porous medium grains and to each other. The transport in this media is usually described by a modified advection-dispersion equation that takes into account the mass exchanges between liquid and solid phase due to physical and physico-chemical interactions:

$$n \cdot \frac{\partial c}{\partial t} + \sum \rho_b \cdot \frac{\partial s_i}{\partial t} + q \cdot \frac{\partial c}{\partial x} - n \cdot D \cdot \frac{\partial^2 c}{\partial^2 x} = 0 \qquad \text{Eq. 1}$$

$$\sum \rho_b \cdot \frac{\partial s_i}{\partial t} = \sum n \cdot k_{att,i} \cdot f_{att,i} \cdot c - \rho_b \cdot k_{det,i} \cdot s_i \qquad \text{Eq. 2}$$

Where c is the colloid concentration in the liquid phase, s is the colloid concentration in the solid phase, n is the porosity of the packed bed, ρ_b is the bulk density of the solid matrix, q is the Darcy velocity, D is the hydrodynamic dispersion coefficient, k_{att} and $k_{det}$are the NP attachment and detachment rate coefficients. The hydrodynamic dispersion coefficient D can be described as:

$$D = \alpha_L \cdot v \qquad \text{Eq. 3}$$

Where α_L is the porous medium dispersivity and v is the pore water velocity.

The first equation (Eq. 1) represents the mass balance for the liquid phase, and the second (Eq. 2) the mass balance for the solid phase and a generalized form for colloid attachment/detachment models.

Furthermore, $\rho_b \cdot \frac{\partial s_i}{\partial t}$ is the general term of non-equilibrium exchange and it describes the mass transfer between the solid and liquid phase. The f_{att} is a function depending on the process or processes described in the following chapters and the i coefficient refers to the active sites: NP retention may be due to more than one (usually, a maximum of two active sites is adopted: i=1,2) (TOSCO ET AL., 2016B). If the porous matrix is homogeneous, only one interaction site type is included in the model. On the contrary, if the solid matrix is supposed to be heterogeneous for the affinity to colloidal particles, more than one site type can be modelled (TOSCO AND SETHI, 2009).

Additionally, clogging due to the accumulation of significant amounts of particles in the pores of the aquifer can be taken into account. This phenomena influence increasing the pressure across the column and reducing the permeability and porosity due to the deposited particles. However, this bachelor's thesis does not consider this phenomenon in the MNMs simulations.

Five mechanisms of colloid deposition in porous media have been identified: clean bed filtration, linear, blocking, ripening and straining. Each of these deposition mechanisms will be discussed below to provide a common reference point and four of them will have the subsequent modelling and discussion.

As is shown in Figure 4, the colloid deposition mechanisms can be classified according to the type of interaction. The linear, blocking and ripening are usually long-term physico-chemical mechanisms, while clean bed filtration and straining are early-term mechanisms.

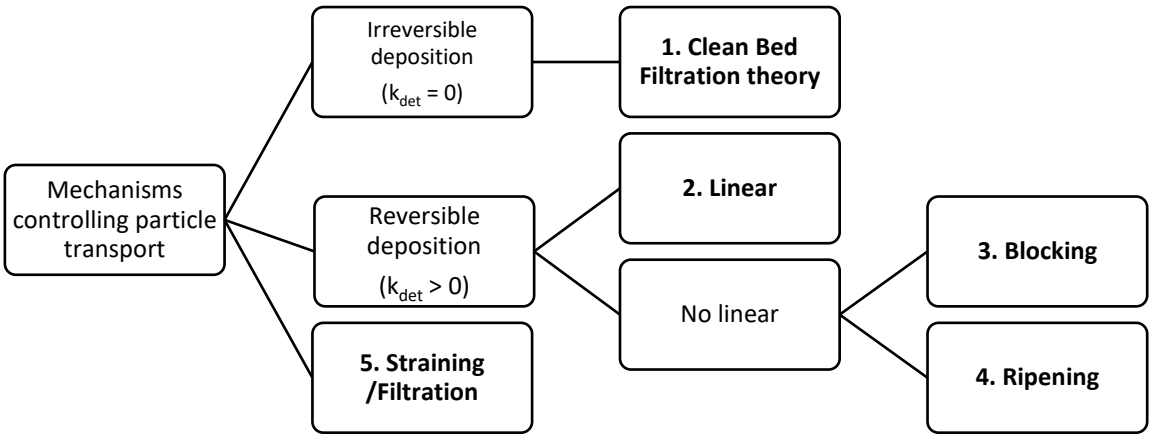

Figure 4. Classification of the colloid deposition mechanisms according to the type of interaction (Source: Own elaboration).

3.1.1 Clean bed filtration

The clean bed filtration, also called classical filtration theory (CFT), is a well-known mechanism of colloid deposition that involves collision with the subsequent retention of colloids at the solid-water interface. This situation is typical in very early stages of attachment. The Figure 5 illustrates how the particles are attached to the pore medium surface.

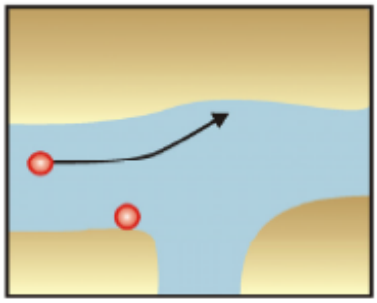

Figure 5. Clean bed filtration pore scale particle retention (Source: Tosco et al., 2014).

It considers a first – order attachment kinetics, while detachment rate coefficient is supposed to be negligible: $k_{det} = 0$ (Tosco and Sethi, 2008). Hence, the interaction is irreversible as described in Figure 4.

CFT was developed from an analysis of colloid attachment to the solid – water interface of a single spherical grain collector and therefore does not include the potential influence of pore structure, grain – grain junctions or surface roughness (Bradford et al., 2006).

This first process mainly describes the attachment to the porous medium surface by the NP. For the clean bed filtration, the term f_{att} in the Eq. 2 is described as simple as:

$$f_{att} = 1 \qquad \text{Eq. 4}$$

Hence, the concentration of retained colloids in porous medium decreases exponentially with depth (Bradford and Bettahar, 2005). Clean bed filtration theory assumes physisco-chemical mechanisms of interaction.

In the theory the k_{att} can be describe as:

$$k_{att} = \frac{3 \cdot (1 - n)}{2 \cdot d_{50}} \cdot \eta \cdot \alpha \cdot q \qquad \text{Eq. 5}$$

Where n is the porosity, d_{50} is the median porous medium grain diameter and q is the Darcyan velocity (Bradford et al., 2006). The other two parameters η (single collector efficiency) and α (colloid attachment efficiency) are widely explained in chapter 3.2.1.

In practice α is usually derived from experimental breakthrough curves, or from fitted values of k_{att} and calculated values of η, although theoretical approaches have also been proposed to predict α (BRADFORD ET AL., 2006).

3.1.2 Linear

The linear mechanism of colloid deposition is ruled by the same principles as the CFT but in this phenomenon, the detachment rate coefficient is not supposed to be negligible: $k_{det} > 0$. Hence, the interaction is reversible as described in Figure 4. Model calculations are performed by assuming that the rate of colloid deposition is independent of previously attached colloids. However, this assumption is only valid for initial deposition rates, when the particles are deposited onto clean collectors. For the linear phenomenon, the term f_{att} in the Eq. 2 is described the same as clean bed filtration theory:

$$f_{att} = 1 \qquad \text{Eq. 6}$$

This mechanism is illustrated in the following figure:

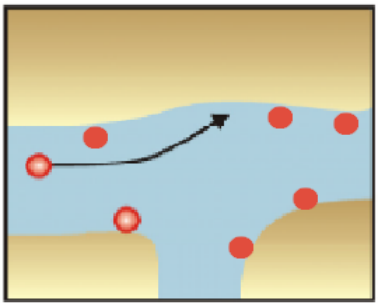

Figure 6. Linear pore scale particle retention (Source: adapted from Tosco et al., 2014).

3.1.3 Blocking

This non-linear particle retention process, also called Langmuir, describes the attachment hindered by other particles as shown in Figure 7.

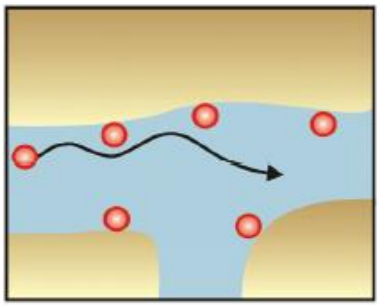

Figure 7. Blocking pore scale particle retention (Source: Tosco et al., 2014).

Model calculations are performed by assuming that initially the rate of colloid deposition is independent of previously attached colloids. However, this assumption could be only valid for initial deposition rates, when the particles are deposited onto clean collectors. The deposition rate may decrease rapidly as particles start to accumulate on the collectors. One explanation for this drop in deposition rate is that as the fraction of the surface covered by colloids increases and deposited colloids may prevent the further attachment of colloids due to a process termed blocking. When blocking is occurring, an attached particle reduces the area available for deposition by an amount that is greater than the projected area of the particle. This mechanism can result in enhanced transport of nanoparticles in porous media (CAMESANO ET AL., 1999).

When blocking occur the colloid concentration in the solid phase is limited to a fixed value s_{max}, hence, the term f_{att} in the Eq. 2 is described according to the Langmuirian approach:

$$f_{att} = 1 - \frac{s}{s_{max}} \qquad \text{Eq. 7}$$

Where s_{max} is the maximum solid phase concentration of attached colloids.

Time dependency in the colloid attachment rate because of blocking can be accounted using Eq. 7 and Eq. 2. During blocking, the value of f_{att} decreases with increasing s as a result of filling of favourable attachment sites such as metal oxide surfaces or clay edges (BRADFORD ET AL., 2006).

3.1.4 Ripening

This phenomenon describes the clustering of attached nanoparticles. Ripening is the process of granular media conditioning during which clean media captures particles and becomes more efficient at capturing additional particles (CRITTENDEN ET AL., 2012). This mechanism is illustrated in the Figure 8.

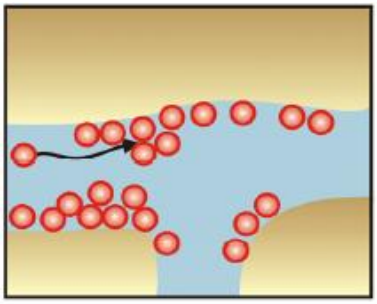

Figure 8. Ripening pore scale particle retention (Source: Tosco et al., 2014).

This non-linear mechanism occurs when attached particles can act as additional collectors for attachment by forming multilayer films (CAMESANO ET AL., 1999).

For ripening process, the term f_{att} in the Eq. 2 is described as:

$$f_{att} = 1 + A_{rip} \cdot s^{\beta rip} \qquad \text{Eq. 8}$$

Where A_{rip} and β_{rip} are fitting parameters. The ripening assumes that f_{att} is a nonlinear function of s.

During ripening f_{att} and consequently k_{att} increases with increasing s due to favourable colloid-colloid interactions. These interactions are between colloids in solution and those attached to grain surfaces (BRADFORD ET AL., 2006).

3.1.5 Straining and filtration

Straining occurs when colloids are retained in pores that are smaller than some critical size, hence, the pores does not always allow the particle transport. However, if this mechanism colloid mobility may still occur in pores that are larger than this critical size as shown in Figure 9.

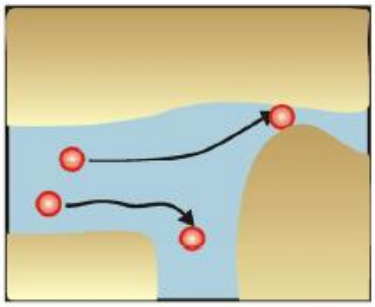

Figure 9. Straining pore scale particle transport (Source: Tosco et al., 2014).

This phenomenon assumes that colloid deposition occurs primarily at the column inlet because the flow field is not yet fully established and colloids therefore have increased accessibility to small pore spaces. Contrary to the previous cases, straining is not a depositions mechanism but a physical mechanism.

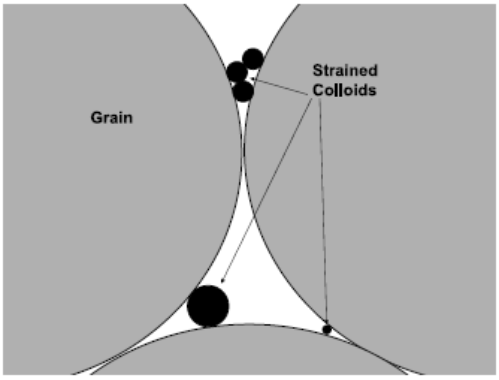

Figure 10. Illustration of strained colloids in the smallest regions of the soil pore space (Source: Bradford et al., 2006).

To better understand and define straining the Figure 10 provides an illustration of strained colloids in the smallest regions of the soil pore space formed adjacent to points of grain-grain contact. In the smallest regions of the pore space the water velocity is very low and these locations can be considered as zones of relative flow stagnation (TORKZABAN ET AL., 2008).

Similar to mechanical filtration (complete retention of colloids at the soil surface), straining of colloids occurs in soil pores and increase with the ratio of the colloid and pore size. In contrast to mechanical filtration, where the particle transport will not occur, straining only occurs in a fraction of the soil pore space (as shown in Figure 10), and colloid transport can still happen in the larger portions of the continuous pore networks.

If the colloid particles are physically excluded from entering all of the soil pores, then complete straining (mechanic al filtration) occurs. In this case, a filter cake or surface mat of colloids forms adjacent to the surface of the porous medium. This filter cake may significantly reduce the permeability of the porous medium-filter cake system. Hence, incomplete straining is the phenomenon that will be studied in this project.

Straining can play an important role in colloid deposition under unfavourable attachment conditions and may explain the limitations of filtration theory. Many environmentally relevant colloids and porous media possess a net negative charge at a neutral pH, and groundwater and surface water resources typically have a low ionic strength. Under these conditions an energy barrier to attachment may occur (unfavourable conditions), and colloids that collide with collector surfaces (soil grains) are not expected to attach to the solid-water interface. In practice, however, a finite number of colloids are retained in porous media even under unfavourable attachment conditions. In contrast to CFT predictions, colloid deposition rates have also frequently been found to vary spatially under unfavourable attachment conditions (BRADFORD ET AL., 2006).

For this process, the term f_{att} in the Eq. 2 is described as:

$$f_{att} = \left[\frac{d_{50} + x}{d_{50}}\right]^{-\beta str} \qquad \text{Eq. 9}$$

Where β_{str} is a fitting parameter that controls the shape of the colloid spatial distribution. Experimental evidence has shown that this parameter con be taken equal to 0.432 with good results (BRADFORD ET AL., 2003). For the remainder of this projectβ_{str} will therefore be fixed to this value.

The term x is the length of the path of the particles in the porous media (in laboratory experiments is the distance travelled from the inlet point) and the value of d_{50} is described as the median grain size of the PM (BRADFORD ET AL., 2006). Therefore, straining is greatest at the column inlet and then is expected to decrease with increasing distance, due to a space-deposition dynamics.

3.2 Factors that influence the NPs transport

The type of interaction mechanisms and the magnitude of attachment and detachment kinetics are strongly influenced by factors that depend on both operative and natural conditions. A NP transport simulation effective tool in assisting the design of a field-scale application of NPs has to take into account these effects in a quantitative, and coupled, way (TOSCO ET AL., 2014). The following subchapters explain the parameters with particular importance.

3.2.1 Sand-particle interactions

The classical filtration theory describes the deposition of particles on the grains of a porous medium (collectors). This phenomenon can be model as a two-step process:

- The transport of the particles from the bulk of the porous medium to the collector surface. Quantified by the single collector contact efficiency η_0; described in chapter 3.2.1.1.
- The adhesion of these particles due to chemical interactions. Described by the attachment efficiency α; described in chapter 3.2.1.2.

The product of these two values (η_0 and α) gives, as a result, the single collector removal efficiency η, which accounts for both the transport and attachment steps (MESSINA ET AL., 2015):

$$\eta = \alpha \cdot \eta_0 \qquad \text{Eq. 10}$$

3.2.1.1 Single collector contact efficiency

The attachment collector efficiency is related to the frequency of colloid collisions on the grain surfaces and accounts for colloid removal due to diffusion, interception, and gravitational sedimentation (LOGAN ET AL., 1995).

Three different deposition mechanisms have been identified whereby particles interact with the sand during the remediation process. It is possible to describe the single collector contact efficiency by sum of the contribution of each mechanisms described. These are considered separately and with classical additivity assumption. Hence, deposition under favourable conditions is shown in Eq. 11:

$$\eta_0 = \eta_G + \eta_I + \eta_D \qquad \text{Eq. 11}$$

- **Gravitational sedimentation** (η_G) due to the settling of the particles when their density is higher than water. This takes account of gravitational forces on the NPs.

The degree of sedimentation mechanism will depend on the ratio v_{NP}/v, where v_p is the velocity of the particle and v is the pore water velocity. Stroke's law is useful equation to understand this phenomenon (BINNIE ET AL., 2009). This law proves that dense and large particles will be more likely to be deposited. Moreover, increasing the fluid velocity decreases the sedimentation effect.

- **Interception** (η_I), which happens when the NP touches a sand grain due to its finite size while moving along a streamline. The probability of this collision will be proportional to d_p/d_{50}, the ratio between the particle and the grain diameter. Thus, the deposition will occur more likely with decreasing the size of the media, or increasing the size of the NP.
- **Brownian diffusion** (η_D), caused by the Brownian thermal movement that determines the divergence of particles from a streamline and brings them to the grain surface, this diffusion causes particle random motion. This mechanism affects significantly only very small particles (BINNIE AND KIMBER, 2009).

It is important to remark that η_0 does not take into account all the interaction forces between particle and collector (Van der Waals forces, repulsive colloidal interactions or electrostatic interactions). The effects of these mechanisms are represented in a simple way in the next figure:

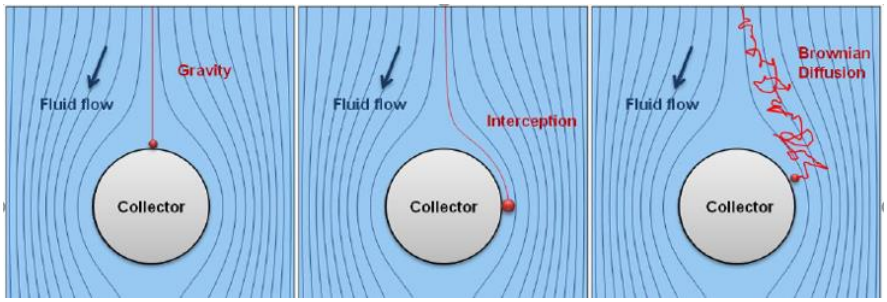

Figure 11. Particle deposition mechanisms (Source: Tosco et al., 2013).

The efficiency of particle removal varies with particle size, a typical variation for three different transport cases from the article MESSINA ET AL, 2015 can be observed in the following figure:

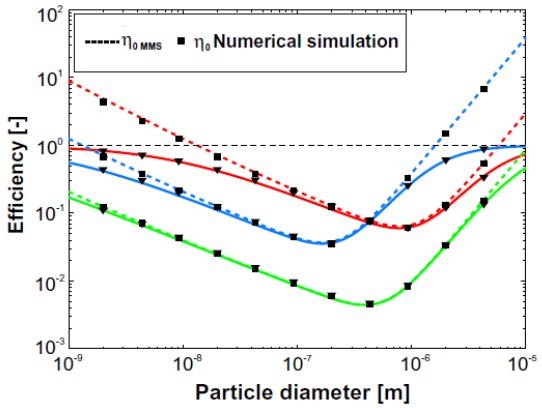

Figure 12. Particle removal efficiency in a granular filter (Source: Messina et al., 2015).

This shows that relative large and relative small particles are removed more efficiently than particles around 1 µm. For the smallest particles, the mechanism that predominates between them and the porous media is diffusion and for the large ones is sedimentation and straining, or commonly called filtration (this mechanism is described with detail in chapter 3.1.5). The effect that predominates for particles around 1 µm is interception and in a lower level sedimentation, and these processes are less effective (BINNIE AND KIMBER, 2009). This removal negatively affects mobility of NPs in the media so it is not a desired for the groundwater remediation.

3.2.1.2 Attachment efficiency

The attachment efficiency α describes the fraction of the particles coming into contact with the collector that actually attaches onto it. This parameter is defined as the ratio of the deposition flux under unfavourable relative to favourable conditions, and it depends on the surface chemistries of the colloids and the grain surfaces. The value of α is typically assumed to be independent of the size of the colloid and the grain surface (LOGAN ET AL., 1995).

3.2.2 Ionic strength

Ionic strength significantly affects the particle-particle and particle-porous medium interactions. As consequence, on a longer period possible changes in the groundwater salt content may lead to immobilization or re-mobilization of the particles, thus affecting their long-term behaviour (TOSCO ET AL., 2016B).

To better understand the role of ionic strength in NPs transport the following figure shows the variation of attachment (k_{att}) and detachment (k_{det}) due to transient ionic strength conditions for blocking mechanism:

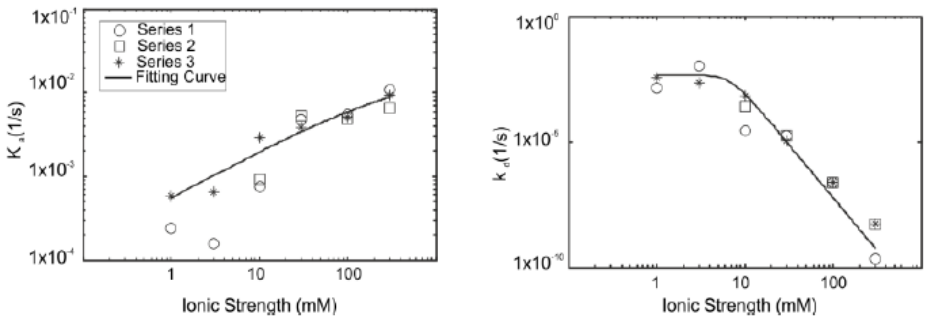

Figure 13. Values of attachment term (left), detachment term (right) as a function of ionic strength in logarithmic scale (Source: adapted from Tosco et al., 2013).

Regarding Figure 13, if the ionic strength is low, it is expected a more important detachment behaviour and when it is high, the attachment will be the more decisive mechanism.

As a general rule, NPs are very mobile at low ionic strength (IS), while increasing salt concentration decreased mobility, and consequently the amount of particles retained in the column increase. Increasing IS result in a retarded breakthrough curve and thus to an increased attachment rate (TOSCO ET AL., 2012).

3.2.3 Fluid viscosity

NPs suspended in water are in most cases not stable and need to be stabilised by addition of polymers in order to be injected into groundwater. Some of the polymers commonly used in field applications are characterized by a non-Newtonian rheological behaviour, which influences the overall injection of the suspension. It is know that particle colloidal stability, and consequently the viscosity of the carrier fluid, significantly affects mobility in the porous medium (TOSCO ET AL., 2016B).

3.2.4 Flow velocity

According to TOSCO ET AL., 2016B during particle injection in a radial geometry, flow velocity decreases hyperbolically with increasing distance from the injection point. Moreover, the flow rate at low IS conditions (when particle deposition rates are low) does not significantly influence the colloid deposition. However, at high IS the effects of flow rate are important for the deposition and release. Generally, particle deposition decreased with increasing flow rate (TOSCO ET AL., 2012).

4 Simulations of the case studies

In this chapter, the MNMs model will be used in order to compare the results obtained in publications with the simulated ones. Moreover, this section shows the differences between four mechanisms of colloid deposition. In all the simulations, the ionic strength is constant and initial conditions of zero concentration of particles in both liquid and solid phase are imposed. It is important to emphasize the fact that all the cases are carried out under different characteristics indicated in each subchapter below.

The type of results studied in the current chapter and provided by the software are:

1. Breakthrough curve: is a graph that simulates the direct measurement of the concentration of nanoparticles (in kg/m^3) in solution in a given point of the column as a function of time. In the simulations of this project is has been taken the concentration at the exit of each column.
2. Ionic strength curve: it provides a graph where is shown the ionic strength (in mM) as a function of time. This project only simulates with constant ionic strength so is used as a tracer curve.
3. Profiles of colloid concentration onto solid phase: this type of graph simulates a scan of the column along its entire length, in order to measure the concentration of nanoparticles (s) present at the end of each injection period.
4. Profile of colloid concentration onto liquid phase: this type of result provides a graph that simulates a scan of the column along its entire length, in order to measure the concentration of nanoparticles (c) in kg/m^3 present at the end of each stress period.

In this project it has been included also a graph that shows the relation between the concentration onto solid and liquid phase versus space, obtained by using a combination of data obtained from the simulation, as explained in the following chapter 4.1.5.

It is important to know that the solutions provided by MNMs are obtained under the assumption of homogeneous porous medium (constant porosity, bulk density and dispersivity) and constant hydrochemical parameters (flow velocity, soil-water partition coefficient, degradation rate).

4.1 Modelling with MNMs 2018

MNMs 2018 (Micro-and Nanoparticle transport, filtration and clogging Model – Suite) is a software tool for the simulation of colloid transport in porous media. It allows simulations of colloid transport in the presence of both constant and transient hydrochemical conditions, with eventual clogging of the porous medium.

This software is usually used in scientific projects for the assisted quantitative analysis of laboratory-scale column tests, and the preliminary design of pilot NP injections in a simplified geometry (radial 1D simulations).

It takes into accounts attachment and detachment phenomena that can be modelled with one or two interaction sites. The deposition phenomenon at each site can be modelled by means of several kinetics: linear, langmuirian ripening and/or straining (described previously).

This software is intended as a complete tool that can provide useful help during all the steps of the design of nanoparticle based remediation, from the particle characterization to the injection design (TOSCO ET AL., 2016B).

The major tools available in MNMs 2018 includes:

- Interaction energy profiles calculation. Which can be used to estimate particle-particle and particle-collector interaction energy profiles using DLVO and Extended-DLVO theory approach. It is usefull to forecast the micro- and nanoparticle behaviour in terms of aggregation and mobility
- Calculation of single collector attachment coefficient (η). That is one of the most important parameters for the assessment of the mobility of micro- and nanoparticles in porous media. MNMs implements a tool to compute η using up to 7 different formulations.
- Simulation of porous medium clogging phenomena. Taking into account the variation of pressure drop along the column due to the medium clogging and solves the differential system coupling flow and transport equations. Porous media clogging occurs when the modification of the column porosity and permeability due to the deposition of colloidal particles strongly influences the flow field and cannot be neglected
- Simulation of particle transport in the presence of Non-Newtonian carrier fluids. NPs suspended in water are generally not stable and need to be stabilized by addition of polymers (Non-Newtonian) in order to be injected in groundwater.
- Simulation of pilot-scale injection of micro and nanoparticles slurries through a single well: radial simulation tool. In field applications, fluids are typically injected into the subsurface via wells or direct push systems, generating a radial flow, with decreasing velocity with increasing distance from the inlet point.
- Simulation of the transport of a dissolved species. Accounting for equilibrium sorption and first order degradation, useful for interpretation of column tracer tests and simulation of contaminant transport.

This last tool of MNMs program is the one used for the current project.

The following subchapters will provide several useful relationships calculations that will be important to understand the chosen parameters for simulations.

4.1.1 Pore volume

One interesting calculation used in the course of the simulations is the conversions between the number of pore volumes (PV) and time (t). Some articles of the bibliography talks about PV and it is essential to change into seconds in order to introduce in the MNMs program.

To know the number of PV:

$$PV = \frac{t \cdot Q}{\pi \cdot r^2 \cdot L \cdot n} = \frac{t \cdot q}{L \cdot n} \quad \text{Eq. 12}$$

Hence, to know the time in second equivalent to 1 PV:

$$t_{1PV} = \frac{\pi \cdot r^2 \cdot L \cdot n}{Q} = \frac{L \cdot n}{q} \quad \text{Eq. 13}$$

Where Q is the discharge rate, q is the Darcyan velocity, n is the porosity, r is the radius and L is the length of the column.

4.1.2 Bulk and grain density

Another used calculation is the relationship between the grain and the bulk density, related for the following equation:

$$\rho_b = \rho_s \cdot (1 - n) \quad \text{Eq. 14}$$

Where ρ_b is the bulk density also called apparent, ρ_s is the grain density and n is the porosity.

This relationship is useful because the MNMs 2018 simulates only with the input of ρ_s and some references use ρ_b.

4.1.3 Retardation factor

It is possible to calculate a theoretical retardation factor equation to zero Eq. 2 and assuming equilibrium values for the concentrations in liquid and solid phase. Hence, in the linear equilibrium model k_{eq} is described as:

$$k_{eq} = \frac{s_{eq}}{c_{eq}} = \frac{k_{att} \cdot \rho_b}{k_{det} \cdot n} \quad \text{Eq. 15}$$

Using the Eq. 15 it can be defined the theoretical retardation factor (VAN GENUCHTEN AT AL., 2012):

$$R_{eq} = 1 + \frac{k_{eq} \cdot \rho_b}{n} = 1 + \frac{k_{att}}{k_{det}} \quad \text{Eq. 16}$$

And can be compared with the experimental one:

$$R_{exp} = \frac{t_{50}}{t_{50,tracer}} \quad \text{Eq. 17}$$

Where t_{50} is the time when the concentration is the half of the initial one and $t_{50,tracer}$ is the same concept but for the tracer test (BRAVACCINI, 2017). The R_{exp} is calculated in all the simulations, not only in linear.

4.1.4 Pore velocity

To ensure correct inputs for the simulations is important to understand the difference between pore velocity (v) and Darcy velocity (q) and the relationship with the porosity (n):

$$v = \frac{q}{n} \quad \text{Eq. 18}$$

4.1.5 Total concentration

A total concentration of NPs by volume of column has been also defined to evaluate cases with a signal of NPs by volume. Hence, a graphic that does not provide the software MNMs is created. It shows the relation between the concentration onto solid and liquid phase versus space:

$$m\ NP_{disolved} = c(x) \cdot V_{disolved} = c(x) \cdot n \cdot V \quad \text{Eq. 19}$$

$$m\ NP_{solid} = m\ solid \cdot s(x) = V \cdot \rho_b \cdot s(x) \quad \text{Eq. 20}$$

$$C^*(x) = \frac{m\ total\ NP}{V} = \frac{m\ NP_{solid} + m\ NP_{disolved}}{V} = \frac{V \cdot \rho_b \cdot s(x) + c(x) \cdot n \cdot V}{V} = \rho_b \cdot s(x) + c(x) \cdot n \quad \text{Eq. 21}$$

Where x is the distance from the inlet of the column, ρ_b is the bulk density of the solid matrix, s is the colloid concentration in the solid phase c is the colloid concentration in the liquid phase, n is the porosity of the packed bed and V is the total volume. For the graphic that correlates the liquid and solid concentration the ordinate axis C* is calculated with Eq. 21 and the abscissa is the column entire length.The following subchapters define the case studies used to validate the simulation.

4.2 Linear case study

This is the first simulation carried out in this project. It has been considered one linear site based on the article TOSCO AND SETHI, 2009. The cited study illustrates the simulation of colloid deposition and release in saturated porous media and the aim is to implement and validate the old version of the program used in this project: MNM1D. The simulation in this subchapter is about colloid deposition of negatively charged latex particles flowing through a saturated sand column.

The following parameters has been taken from the article:

Table 1. Properties for the simulation of the linear mechanism (Source: Tosco and Sethi, 2009).

Parameter	***Parameter explanation***	***Value***	***Units***
L	Column length	0,1	m
q	Darcyan Velocity	$8 \cdot 10^{-5}$	m/s
α_L	Dispersivity	$1 \cdot 10^{-7}$	m
n	Clean Bed effective porosity	0,4	-
ρ_s	Grain density of the sand	1500	kg/m^3
k_{att}	Attachment coefficient	$8 \cdot 10^{-3}$	s^{-1}
k_{det}	Detachment coefficient	$4 \cdot 10^{-3}$	s^{-1}
IS	Ionic Strength	1	mM
t_{inj}	Injection time	3600	s
C_{in}	Injection concentration	1	g/l
C_0	Initial concentration inside column	0	g/l

The time equivalent to 1 PV is calculated below:

$$t_{1PV} = \frac{L \cdot n}{q} = \frac{0{,}1 \cdot 0{,}4}{8 \cdot 10^{-5}} = 500\ s$$

Moreover, modifying the temporal discretization of the injections, the model can provide profiles that helps in some way, depending on the suitability of the chosen time discretization, understanding the phenomenon that is simulated. The stress periods time chosen are the following:

Table 2. Stress period time for linear simulation.

Stress Period	1	2	3	4	5	6
Δt [s]	300	700	500	500	1000	600
t [s]	300	1000	1500	2000	3000	3600

Once all the parameters are introduced in the MNMs program, the result is the following breakthrough graph that shows the ionic strength as a tracer (green) and the linear simulation of particle concentration vs time (blue):

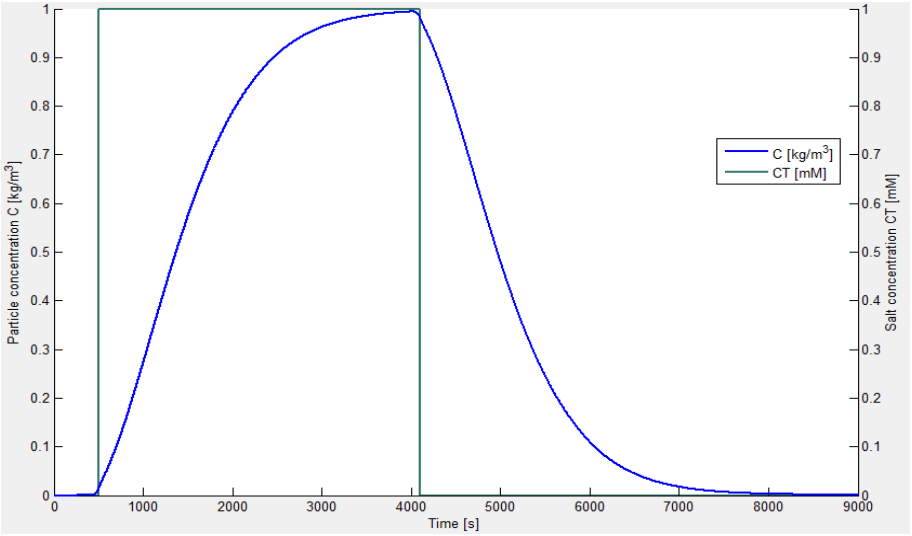

Figure 14. Simulated breakthrough curve for colloid transport in linear site.

The following graph form the article cited in this subchapter is shown to compare and validate the simulation with MNMs 2018:

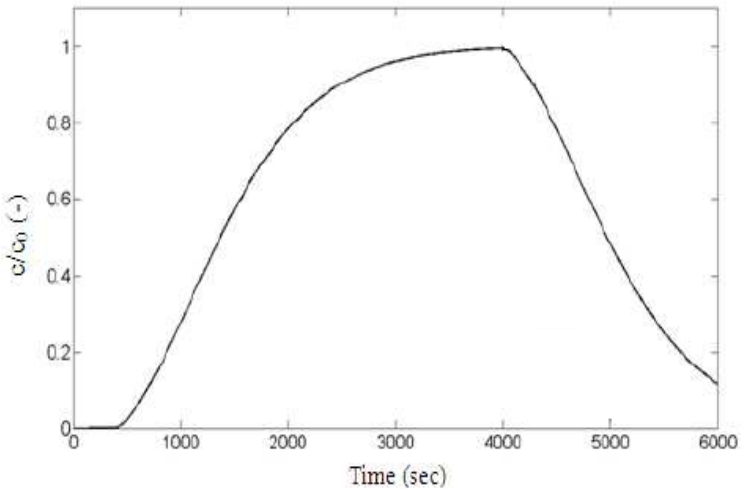

Figure 15. Simulated breakthrough curve in MNM1D (Source: Tosco and Sethi, 2009).

Both breakthrough curves (Figure 14 and Figure 15) has an increasing trend until reaching their highest concentration in C ≈ C0. The simulation maximum value coincides with the tracer one. Afterwards, when there is no more injection of nanoparticles, a decline until reaching C = 0 kg/m^3 is observed.

For the MNMs simulation, the peak time is 4016 seconds and this value can be compared with the one graph from Tosco and Sethi, 2009. Unfortunately, the data from the article graph is not available so the comparison cannot be numerical, but qualitative. Hence, both charts has the peak at the same time approximately. Another interesting comparison is the two times where the concentration is the 50% from the total. For the MNMs simulation this times are 1364 s from the growth period and 4972 for the decreasing term. Visually comparing with the graph from the article is possible to affirm that those points are approximately coincident. In conclusion, the similarity between both curves validates the linear simulation with MNMs 2018.

The retard factor can be calculated, with Eq. 16 and Eq. 17, in a theoretical (assuming equilibrium) and experimental way. The following results are quite similar so the theory agrees with the MNMs simulation:

$$R_{eq} = 1 + \frac{k_{att}}{k_{det}} = 1 + \frac{8 \cdot 10^{-3}}{4 \cdot 10^{-3}} = 3$$

$$R_{exp} = \frac{t_{50}}{t_{50,tracer}} = \frac{1364}{500} = 2{,}73$$

Another interesting graph that MNMs provides is the profile of colloid concentration onto solid phase. Each curve is the concentration at the end of each stress period described in Table 2.

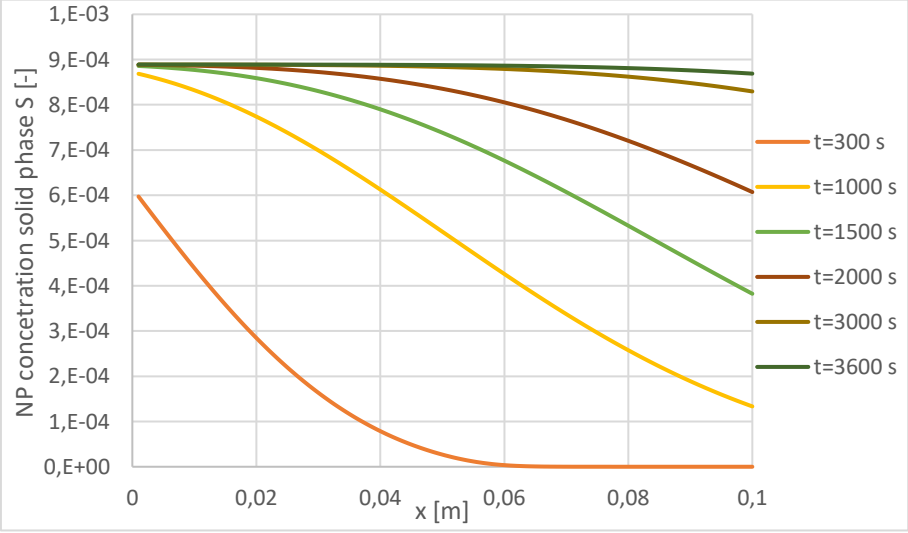

Figure 16. Profile of colloid concentration onto solid phase vs the distance along the column in linear site.

Another chart obtained is the profile of colloid concentration onto liquid phase at the end of the same stress periods as before:

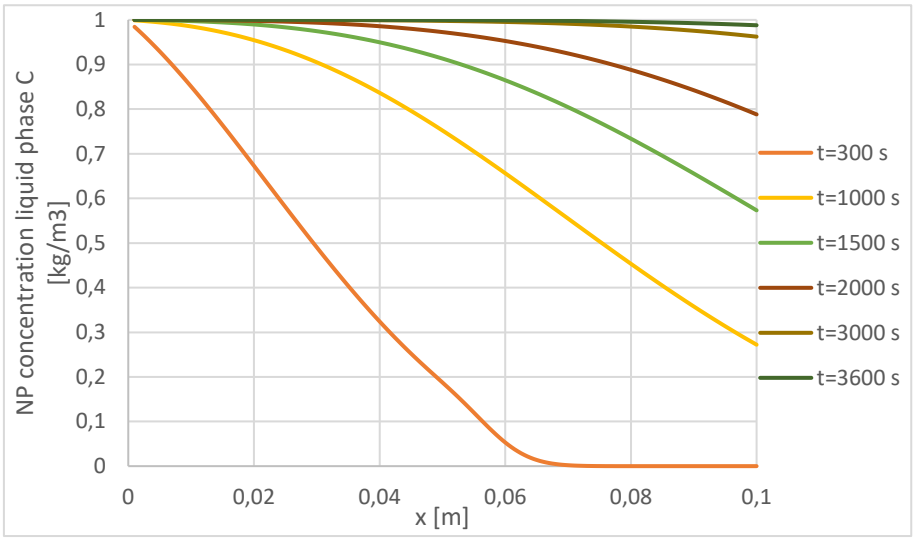

Figure 17. Profile of colloid concentration onto liquid phase vs the distance along the column in linear site.

Finally exporting the data into excel, is possible to create a graph that the program does not include and it is interesting to know if the column deposition of colloids occurs more in the solid or liquid phase. The ordinate axis of this graph is defined as: $C^* = \rho_b \cdot s + c \cdot n$

The meaning of C* is to create an own elaboration graph with the data from the MNMs simulation that represents the total concentration of NPs (solid and liquid phase) for each column volume.

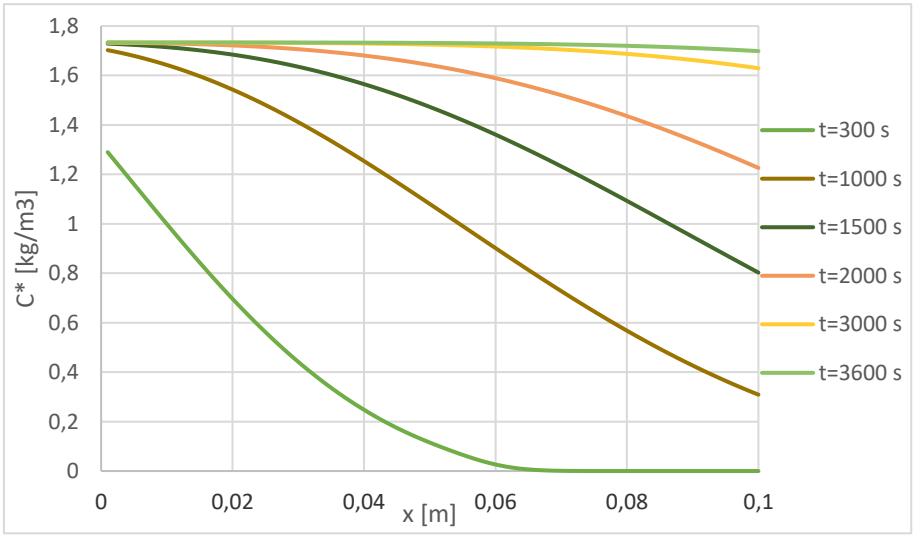

Figure 18. Profile of total colloid concentration vs distance along the column in linear site.

Comparing the similarities and differences between the Figure 18 and both concentration profiles provided by MNMs is it possible to conclude in a qualitative way that the concentration in liquid

phase is mayor in the experiment due the equal shape of Figure 18 and Figure 17. The solid phase nanoparticles (s) are less than the liquid ones at the end of the injection periods.

To validate in a numerical way it has been calculated a percentage of NPs in liquid phase in four chosen time curves:

$$Liquid\ phase\ NPs\ [\%] = \frac{n \cdot C}{C^*} \cdot 100 \qquad \text{Eq. 22}$$

The graph obtained is the following:

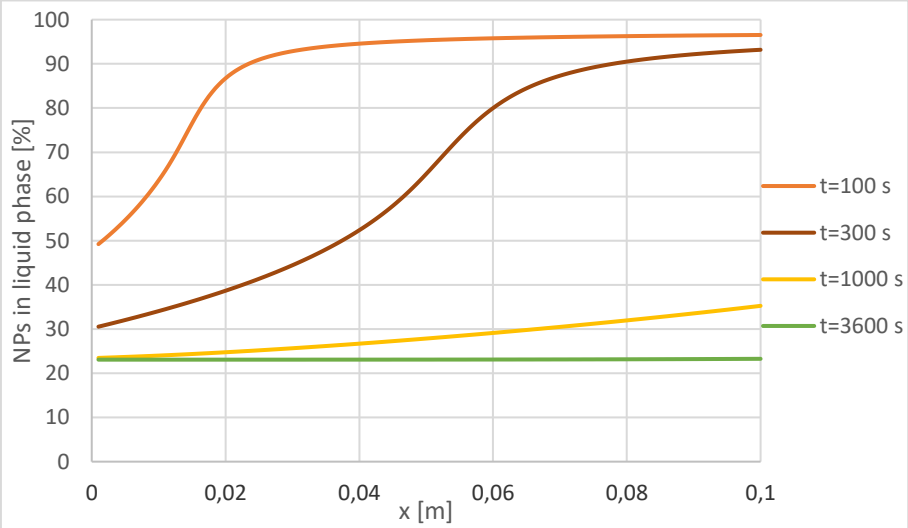

Figure 19. Liquid ratio vs distance along the column in linear site for four chosen times.

The chart depicts that the percentage of NPs in liquid phase is bigger at the beginning of the simulation; hence, adsorption predominates and concentration in water decreases with time. The last periods has more deposited NPs in solid phase as it is shown in Figure 19.

4.3 Blocking case study

For the Langmuir simulation, it has been used the parameters from the article Tosco et al., 2016a, which assumes a single-site reversible blocking deposition. The aim of the work is to study the influence of flow velocity and ionic strength for two different carbon-based NPs and validate the 3D modelling tool from MNMs. The used nanoparticles for blocking simulation are Single Layer Graphene Oxide (SLGO) with a nominal size 300-800 nm. The article verify the suitability of colloid transport equations for this nanoparticles against experimental data of column transport tests, and the results are up-scaled to simulate a spill of waste water containing SGLO in a heterogeneous 3D aquifer system. The parameters used in the simulation are:

Table 3. Properties for the simulation of the blocking mechanism (Source: Tosco et al., 2016a).

Parameter	***Parameter explanation***	***Value***	***Units***
L	Column length	0,111	m
r	Radius of the column	0,008	m
Q	Discharge rate	$1{,}56 \cdot 10^{-8}$	m^3/s
α_L	Dispersivity	$6{,}17 \cdot 10^{-3}$	m
n	Clean Bed effective poros8ity	0,45	-
ρ_s	Grain density of the sand	1201	kg/m^3
k_{att}	Attachment coefficient	$1{,}64 \cdot 10^{-4}$	s^{-1}
k_{det}	Detachment coefficient	$8{,}6 \cdot 10^{-4}$	s^{-1}
s_{max}	Maximum blocking concentration	$2{,}17 \cdot 10^{-6}$	-
IS	Ionic Strength	0,1	mM
t_{inj}	Injection time	5,5	PV
C_{in}	Injection concentration	10	g/l
C_0	Initial concentration	0	g/l

The time equivalent to 1 PV is calculated and afterwards the injection time in seconds to simulate:

$$t_{inj} = t_{1PV} \cdot n^{\underline{o}}\, PV = \frac{\pi \cdot r^2 \cdot L \cdot n}{Q} \cdot n^{\underline{o}}\, PV = \frac{\pi \cdot 0.008^2 \cdot 0{,}111 \cdot 0{,}45}{1{,}56 \cdot 10^{-8}} \cdot 5{,}5 = 3496\ s$$

The stress periods time are the following:

Table 4. Stress period time for blocking simulation.

Stress Period	**1**	**2**	**3**	**4**	**5**	**6**
Δt [s]	100	200	700	1000	1000	496
t [s]	100	300	1000	2000	3000	3496

Once all the parameters are introduced, the breakthrough curve obtained is:

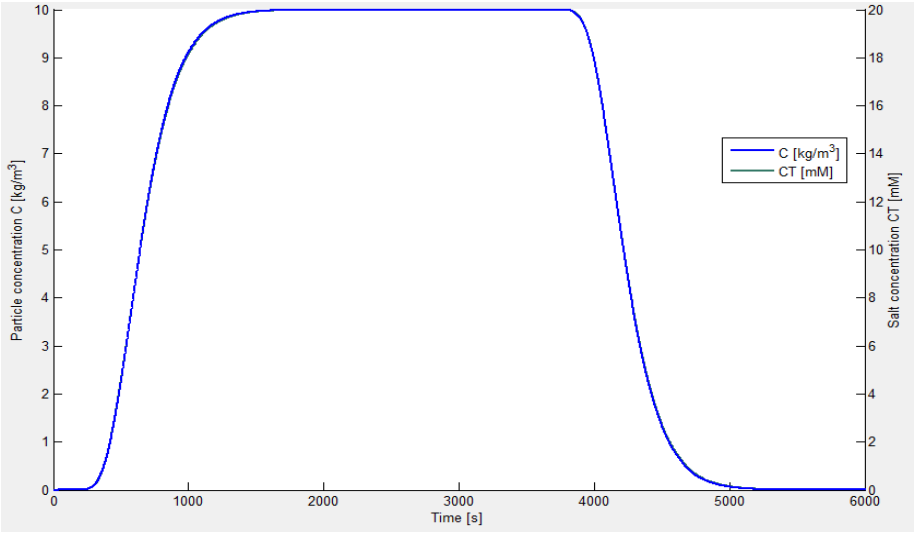

Figure 20. Simulated breakthrough curve for colloid transport in blocking site.

The following graph form the article cited in this subchapter is shown to compare visually:

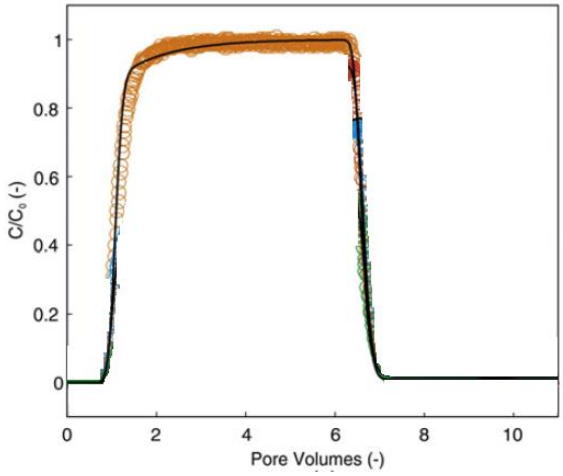

Figure 21. Simulated breakthrough curve for SLGO nanoparticles using MNMs (Source: adapted from Tosco et al., 2016a).

In this case, the tracer curve in the Figure 20 is not visible because it follows exactly the points of the breakthrough curve. This phenomenon is due to the low ionic strength in this experiment (0,1 mM) that causes a lower attachment and a higher detachment as explained in chapter 3.2.2.

Both breakthrough curves have an increasing trend until reaching their highest concentration in C ≈ C0, like in the linear site. Afterwards, when there is no more injection of nanoparticles, a decline until reaching C = 0 kg/m^3 is observed.

The injection time for the article graph is 5,5 PV and for the MNMs simulation it has been introduced the equivalent time in seconds. Unfortunately, the data from the article graph is not available so

the comparison cannot be numerical, but qualitative. Hence, both charts have the maximum during the same time approximately.

The two times where the concentration is the 50% from the total can be interesting in order to compare the breakthrough curves. For the MNMs simulation this times are 644 s from the growth period and 4240 s for the decreasing term. To compare is needed the change to PV using Eq. 12:

$$PV_{50\%\,1} = \frac{644 \cdot 1{,}56 \cdot 10^{-8}}{\pi \cdot 0.008^2 \cdot 0{,}111 \cdot 0{,}45} = 1\ PV$$

$$PV_{50\%\,2} = \frac{4240 \cdot 1{,}56 \cdot 10^{-8}}{\pi \cdot 0.008^2 \cdot 0{,}111 \cdot 0{,}45} = 6{,}59\ PV$$

Visually comparing with the graph from the article is possible to affirm that those points are approximately coincident. In conclusion, the similarity between both curves validate the linear simulation with MNMs 2018.

It can also be calculated with Eq. 17 the experimental retardation factor as shown below:

$$R_{exp} = \frac{t_{50}}{t_{50,tracer}} = \frac{644}{644} = 1$$

Another interesting graph that the program MNMs provides is the profile of colloid concentration onto solid phase. Each curve is the concentration at the end of the stress periods from Table 4:

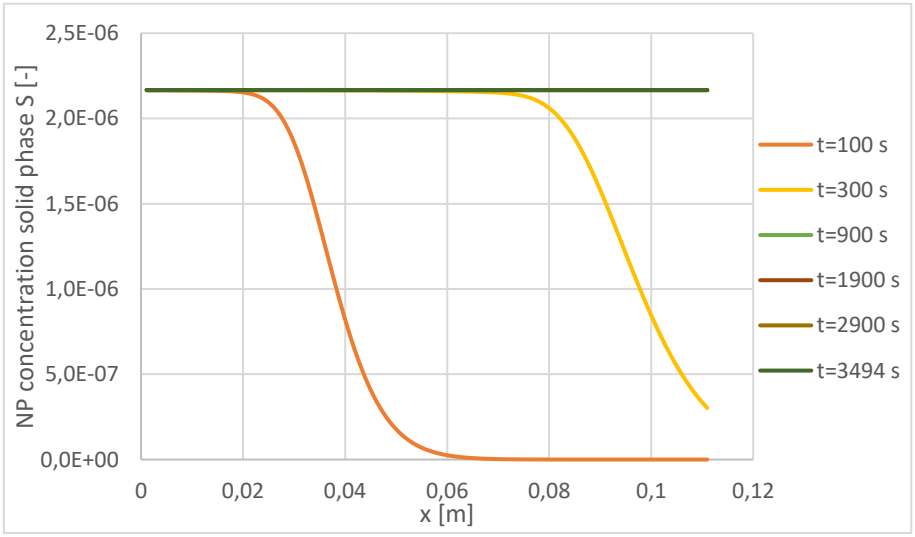

Figure 22. Profile of colloid concentration onto solid phase vs the distance along the column in blocking site.

The maximum value for this graph is $2{,}17 \cdot 10^{-6}$ that represents the maximum blocking concentration in solid phase (s_{max}) and coincides with the introduced for the simulation.

Another chart obtained is the profile of colloid concentration onto liquid phase at the end of the same stress periods as before:

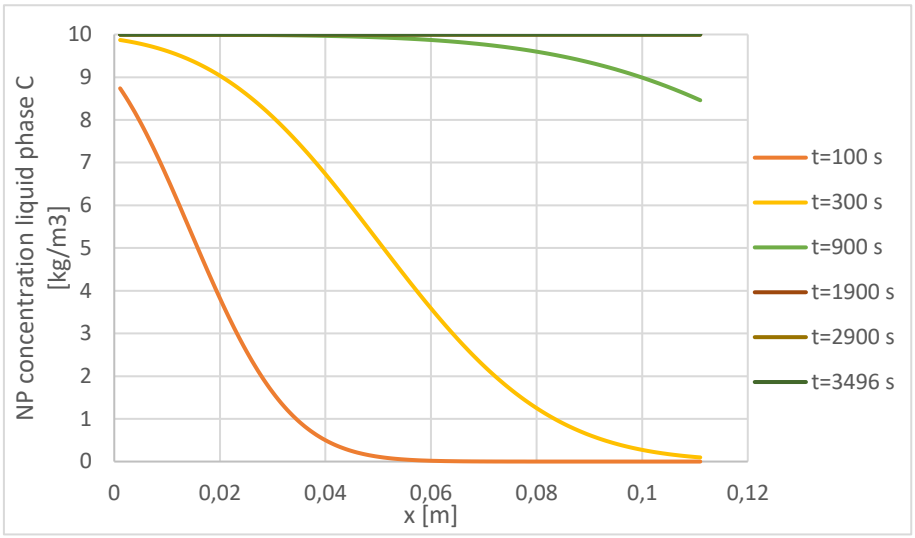

Figure 23. Profile of colloid concentration onto liquid phase vs the distance along the column in blocking site.

Finally exporting the data of the blocking simulation into excel, is possible to obtain a graph that the program does not provide where Eq. 21 defines the ordinate axis: $C^* = \rho_b \cdot s + c \cdot n$

The information obtained from this chart is the phase (liquid or solid) of the deposited colloids inside the column. The term C* represents the total concentration of NPs for each column volume.

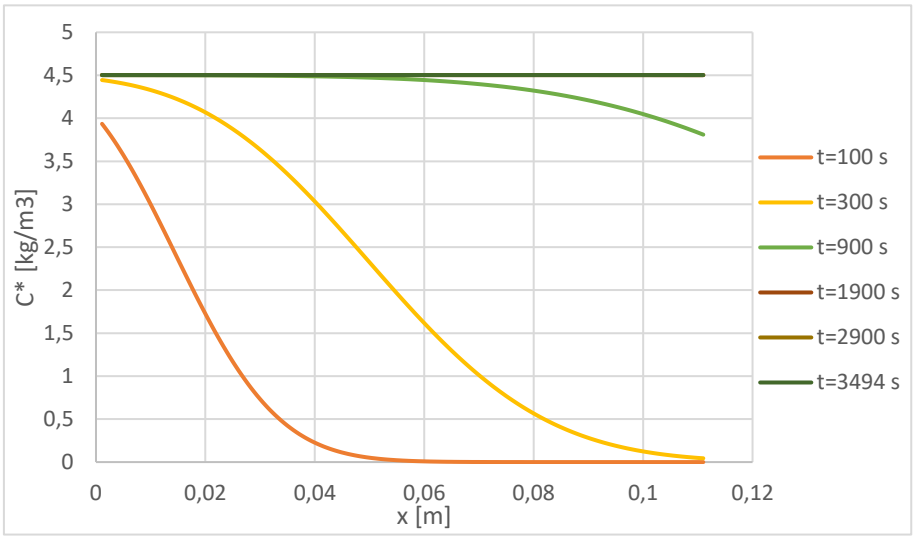

Figure 24. Profile of colloid concentration in solid and liquid phase vs distance along the column in blocking site.

Comparing the similarities and differences between the Figure 24 and both concentration profiles (Figure 22 and Figure 23) is it possible to conclude that the experiment has more concentration of

nanoparticles in liquid phase. This qualitative conclusion has been done because of the closeness shape between Figure 24 and the profile of colloid concentration in liquid phase.

A numerical path to be sure about the phase (liquid or solid) of the deposited NPs is to calculate the value of $\rho_b \cdot s_{max} = 2{,}6 \cdot 10^{-3}$ kg/m^3 and it is clear that is negligible when calculating C^*. Hence, the solid phase NPs are imperceptible compared with the liquid ones.

4.4 Ripening case study

In this case study, the used article is HOSSEINI AND TOSCO, 2013 due to the assumption of ripening in the nanoparticle transport. The aim of the work is to study the mobility of bimetallic NPs dispersions. In particular, the influence of flow rate and the injection of particle concentration. An interesting point is to prove that concentrated colloidal suspensions of NZVI deposition does not follow linear, irreversible kinetics like those considered in the clean bed filtration theory, and ripening deposition dynamics is observed.

The nanoparticles used are constituted by a core of Fe^0 partly coated by Cu, named as nano-Fe/Cu particles with a particle diameter equal to 70 ± 5 nm. The presence of a partial coating of Cu was found to be responsible for longer reactivity lifetime, along with prevention or reduction of the formation and accumulation of toxic by-products. In pre-conditioning and flushing steps, the natural groundwater of Karaj city (Iran) with ionic strength of 40 nm was used.

It has been chosen a low concentration of nanoparticles (from all the different cases in the same article) in order to avoid the influence of clogging phenomenon due to deposition of particles and the decrease of the pore pressure variation during the injection period in the column.

Furthermore, when the concentration is low the main site is considered single and ripening, even though the article talks about two sites.

The parameters used in the simulation are:

Table 5. Properties for the simulation of the ripening mechanism (Source: Hosseini and Tosco, 2013).

Parameter	***Parameter explanation***	***Value***	***Units***
L	Column length	0,5	m
r	Radius of the column	0,0125	m
v	Pore water velocity	$2 \cdot 10^{-3}$	m/s

α_L	Dispersivity	$5{,}7 \cdot 10^{-3}$	m
n	Clean Bed effective porosity	0,37	-
ρ_s	Grain density of the sand	2650	kg/m^3
k_{att}	Attachment coefficient	$1{,}3 \cdot 10^{-2}$	s^{-1}
k_{det}	Detachment coefficient	$3{,}9 \cdot 10^{-2}$	s^{-1}
A_{rip}	Ripening multiplier	4000	-
β_{rip}	Ripening exponent	1,51	-
IS	Ionic Strength	40	mM
t_{inj}	Injection time	1050	s
C_{in}	Injection concentration	2	g/l
C_0	Initial concentration	0	g/l

In the article cited there are three different pore water velocities for the 2 g/l concentration and it has been chosen the higher one to avoid the sedimentation effect explained in chapter 3.2.1.1.

The MNMs program required the input of Darcy velocity so Eq. 18 is used:

$$q = v \cdot n = 2 \cdot 10^{-3} \cdot 0{,}37 = 7{,}4 \cdot 10^{-4}\ m/s$$

The time equivalent to 1 PV is calculated below:

$$t_{1PV} = \frac{L \cdot n}{q} = \frac{0{,}5 \cdot 0{,}37}{7{,}4 \cdot 10^{-4}} = 250\ s$$

The stress periods time chosen are the following:

Table 6. Stress period time for ripening simulation.

Stress Period	**1**	**2**	**3**	**4**	**5**
Δt [s]	200	200	200	400	50
Time [s]	200	400	600	1000	1050

Once all the parameters are introduced in the MNMs program, the result is the following breakthrough graph that shows the ionic strength as a tracer (green) and the linear simulation of particle concentration vs time (blue):

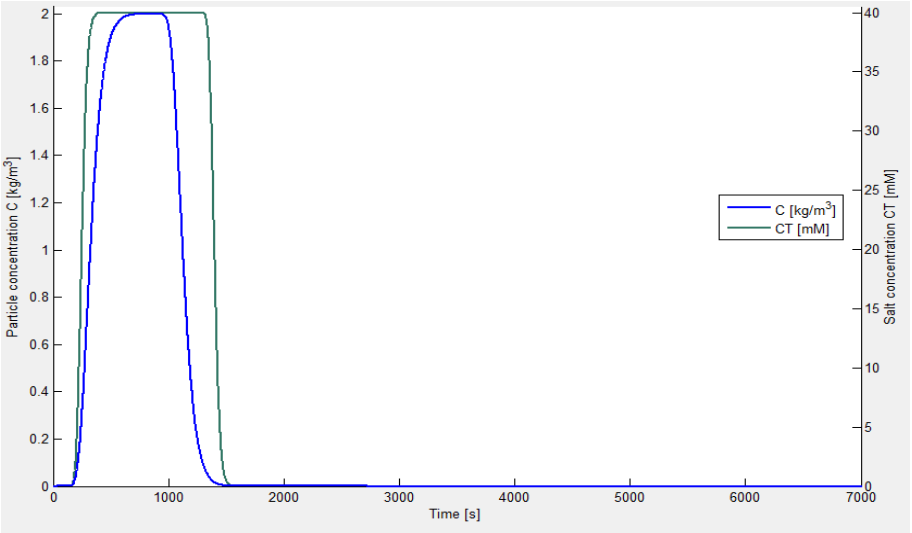

Figure 25. Simulated breakthrough curve for colloid transport in ripening site.

The following graph form the article cited in this subchapter is shown to compare with the blue line from Figure 25:

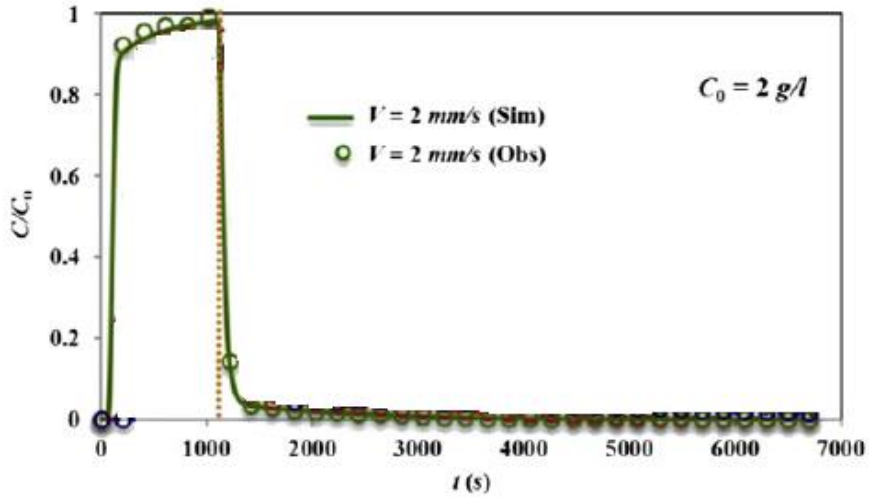

Figure 26. Simulated breakthrough curve for nZVI particles (Source: adapted from Hosseini and Tosco, 2013).

One of the similarities between the ripening breakthrough curves are that at the beginning of the injection period there is a fast increase trend until reaching almost the injection concentration in a short interval of time. Moreover, after the injection time, a decline until reaching C = 0 kg/m^3 is observed.

However, in the article graph the maximum is not attained for an interval of time (as the simulation), but for only a specific time. Unfortunately, the data from the article graph is not available so the maximum time cannot be exactly, but approximately, it can be defined as 1050 s. Hence, the injection time matches the maximum time.

Furthermore, the origin of coordinates for the article graph is not corresponding to the beginning of the injection due to the fast breakthrough. For this reasons it is possible to conclude that the article authors ruled out the first data times. This cause a displacement in time between both breakthrough curves as described below.

Another interesting comparison is the two times where the concentration is the 50% of the total. For the MNMs simulation this times are 324 s from the growth period and 1328 for the decreasing term, so Δt= 1004 s. Visually comparing with the graph from the article is possible to affirm that Δt is the same. Nonetheless, as commented before, the data are displaced in time and that can be an explanation for the non-coincident times but coincident time increment.

This article also provides a graph about the tracer breakthrough curve and to compare properly it was necessary to adapt the x-axis tracer chart from the MNMs simulation as shown below:

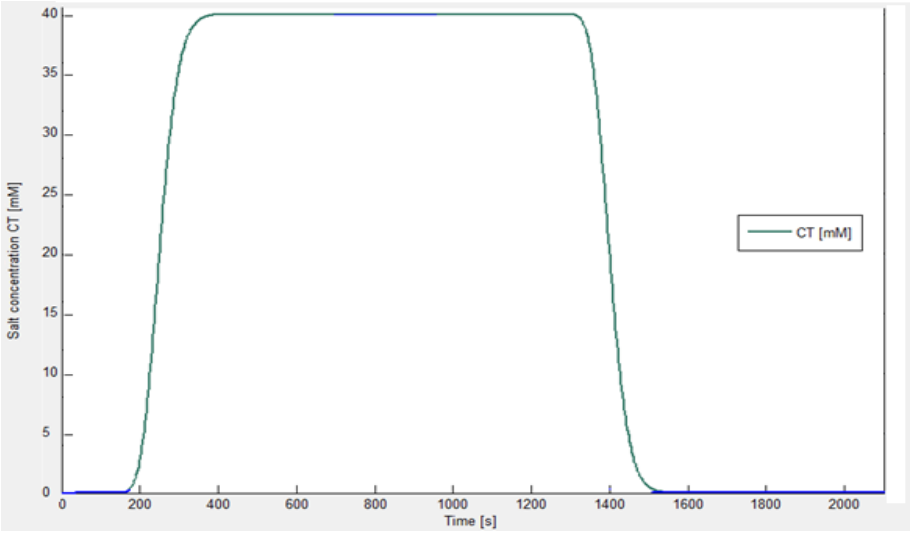

Figure 27. Simulated breakthrough curve for NaCl tracer in ripening site.

Beneath is shown the graph that the cited article provides for the tracer test:

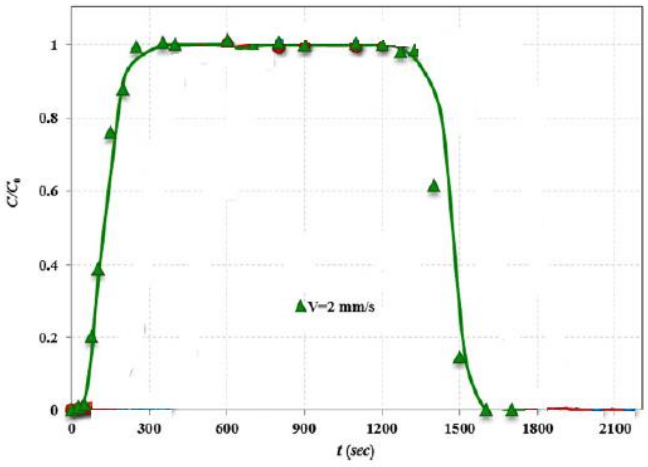

Figure 28. Simulated breakthrough curve for NaCl tracer (Source: adapted from Hosseini and Tosco, 2013).

Both tracer curves has the same silhouette. Nonetheless, there two main differences, the first is the displacement in time commented before in this chapter. The second is the two times where the concentration is the 50% of the total. For the MNMs simulation this times are 250 s from the growth period and 1500 for the decreasing term, so Δt= 1250 s. In contrast to the article tracer curve that has Δt= 1300 s.

The retardation experimental factor can be calculated for this ripening simulation in MNMs assuming equilibrium using Eq. 17:

$$R_{exp} = \frac{t_{50}}{t_{50,tracer}} = \frac{324}{250} = 1{,}3$$

Another interesting chart that is provided by the simulation is the profile of colloid concentration onto solid phase:

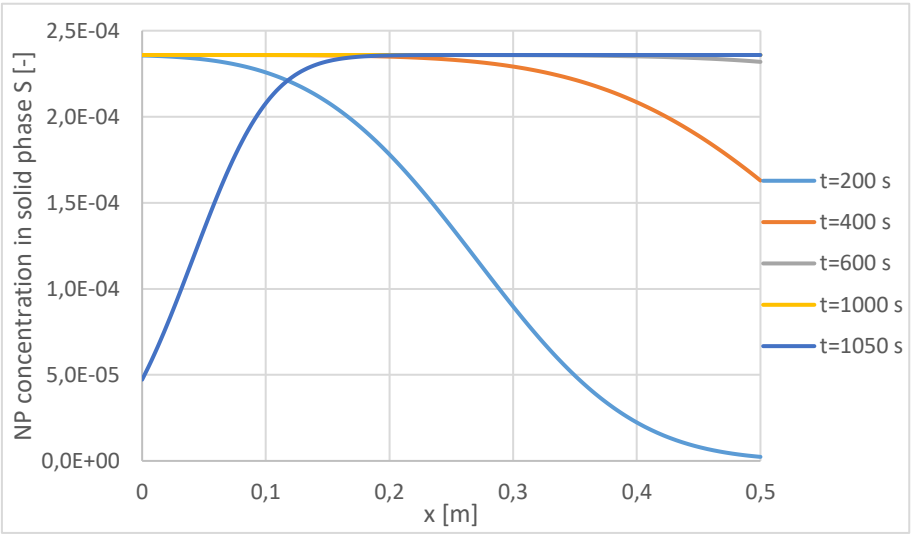

Figure 29. Profile of colloid concentration onto solid phase vs the distance along the column in ripening site.

The profile of colloid concentration onto liquid phase provided by MNMs can be observed below:

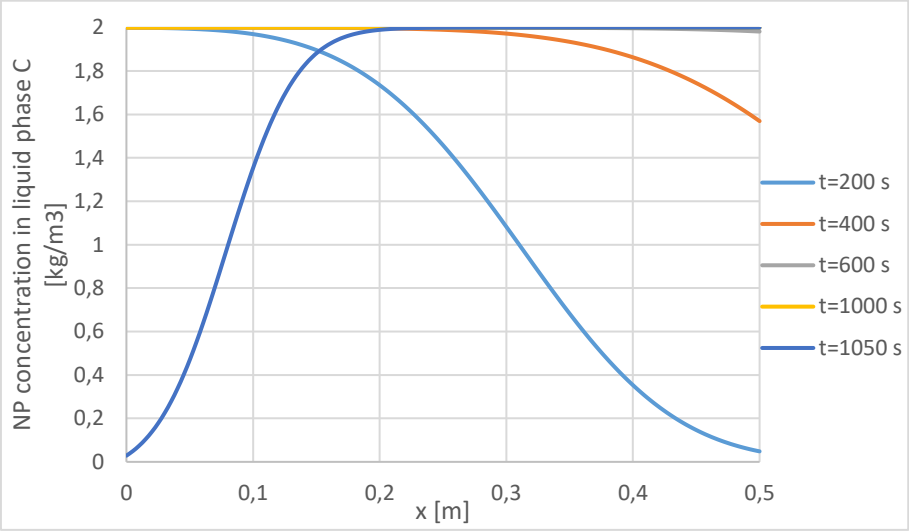

Figure 30. Profile of colloid concentration onto liquid phase vs the distance along the column in ripening site.

Finally exporting the data into excel, is possible to create a graph that the program does not include and it is interesting to know if the column deposition of colloids occurs more in the solid or liquid phase. The ordinate axis of this graph is defined in Eq. 21 and the abscissa axis is the distance along the column in meters.

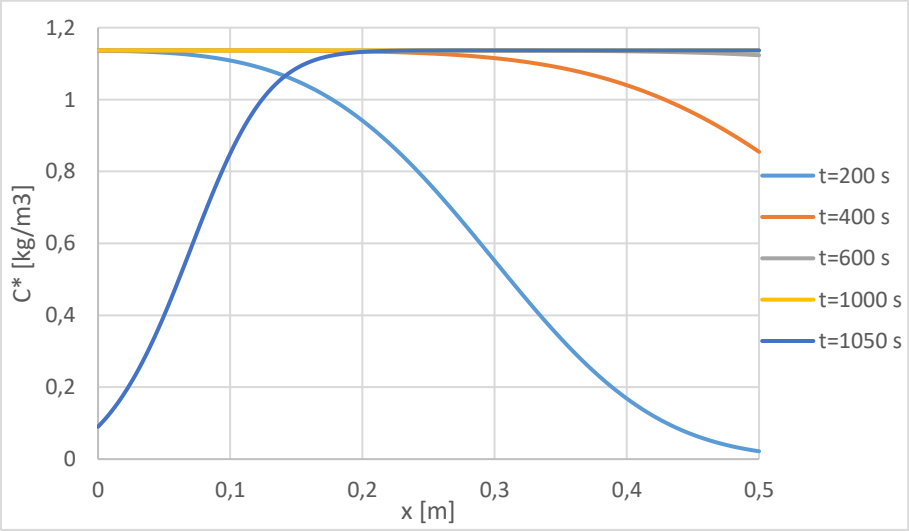

Figure 31. Profile of colloid concentration in solid and liquid phase vs distance along the column in ripening site.

For this simulation k_{att} and k_{det} are big enough to assume that the data approaches to equilibrium between the NP concentration in solid and liquid phase. The kinetics for this case is fast hence, the total concentration graph C* is expected to be similar to C and S charts.

It has been calculated a percentage of NPs in liquid phase for the five stress periods with Eq. 22 and the graph obtained is the following:

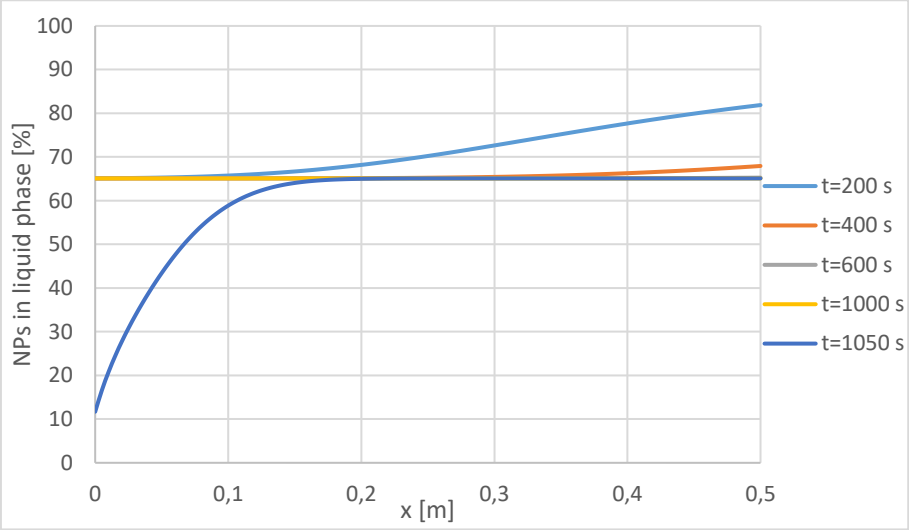

Figure 32. Liquid ratio vs distance along the column in linear site for four chosen times.

The chart depicts that the percentage of NPs in liquid phase is bigger in the major part of the injection period; this is due to an adsorption behaviour and the low attachment. However, the last period has more deposited NPs in solid phase in the inlet point because it is the last injection time and hence afterwards there is no more injection concentration.

4.5 Straining case study

For this case study, the straining mechanism has been simulated with the parameters from the article TORKZABAN ET AL., 2008.

The article is about a series of column experiments that were undertaken to explore the influence of water saturation, pore-water ionic strength and grain size on the transport of latex microspheres in porous media. Straining – the retention of colloids in low velocity regions of porous media such as grain junctions – was the primary mechanism of colloid retention.

The mechanism simulated was observed when most colloids were found deposited close to the column inlet, and hyper-exponential deposition profiles were observed. High unfavorable attachment conditions were employed to ensure a strong repulsive energy barrier against attachment and therefore the retention mechanism involved were not attachment by simply chemical interactions, but rather by straining.

The nanoparticles used are spherical Carboxylate-modified latex (CML) colloids with a particle size of 1100 nm, chosen due to the high density of carboxylic acids on the colloid surface creating a

negatively charged-hydrophilic surface. The size of the nanoparticles validate that the dominant deposition mechanism is straining.

The summary of the parameters for this simulation can be seen below:

Table 7. Properties for the simulation of the straining mechanism (Source: Torkzaban et al., 2008).

Parameter	***Parameter explanation***	***Value***	***Units***
L	Column length	0,1	m
v	Pore water velocity	$6{,}5 \cdot 10^{-5}$	m/s
α_L	Dispersivity	$1 \cdot 10^{-3}$	m
n	Clean Bed effective porosity	0,25	-
ρ_s	Grain density of the sand	2650	kg/m^3
d_{50}	Mean diameter of sand grains	$2{,}4 \cdot 10^{-4}$	m
k_{att}	Attachment coefficient	$2{,}8 \cdot 10^{-3}$	s^{-1}
k_{det}	Detachment coefficient	$1{,}33 \cdot 10^{-4}$	s^{-1}
β_{str}	Straining fitting parameter	0,432	-
IS	Ionic Strength	30	mM
t_{inj}	Injection time	2,7	PV
C_{in}	Injection concentration	$2{,}65 \cdot 10^{7}$	Colloids/ml
C_0	Initial concentration	0	g/l

The MNMs program required the input of Darcy velocity, with the Eq. 18 is used:

$$q = v \cdot n = 6{,}5 \cdot 10^{-5} \cdot 0.25 = 1{,}62 \cdot 10^{-5}\ m/s$$

The MNMs program required the input of injection concentration in g/l (equal to kg/m^3), so a conversion was needed for this simulation using the following equation:

$$\frac{mass}{volume} = \frac{number\ of colloids}{V} \cdot V_p \cdot \rho_p \qquad \text{Eq. 23}$$

Assuming homogeneous distribution of particles, where V_p is the volume for one spherical particle and ρ_p is the colloids density.

$$\frac{mass}{volume} = \frac{2{,}65 \cdot\ 10^7\ colloids}{10^{-6}\ m^3} \cdot \frac{4}{3} \cdot \pi \cdot \left(\frac{1{,}1 \cdot 10^{-6} m}{2}\right)^3 \cdot \frac{0.001055\ kg}{10^{-6}\ m^3} = 0{,}02\ kg/m^3$$

The time equivalent to 1 PV is calculated dividing the length of the column and the pore water velocity as shown below:

$$t_{1PV} = \frac{L}{v} = \frac{0{,}1}{6{,}5 \cdot 10^{-5}} = 1538{,}46\ s$$

Thus, the injection time in seconds for this simulation is:

$$t_{inj} = 2{,}7\ PV \cdot \frac{1538{,}46\ s}{1\ PV} = 4154\ s$$

The stress periods time are the following:

Table 8. Stress period time for straining simulation.

Stress Period	**1**	**2**	**3**	**4**	**5**	**6**
Δt [s]	200	800	500	1000	1000	664
Time [s]	200	1000	1500	2500	3500	4154

Once all the parameters are introduced in the MNMs program, the result is the following breakthrough graph that shows the ionic strength as a tracer (green) and the linear simulation of particle concentration vs time (blue).

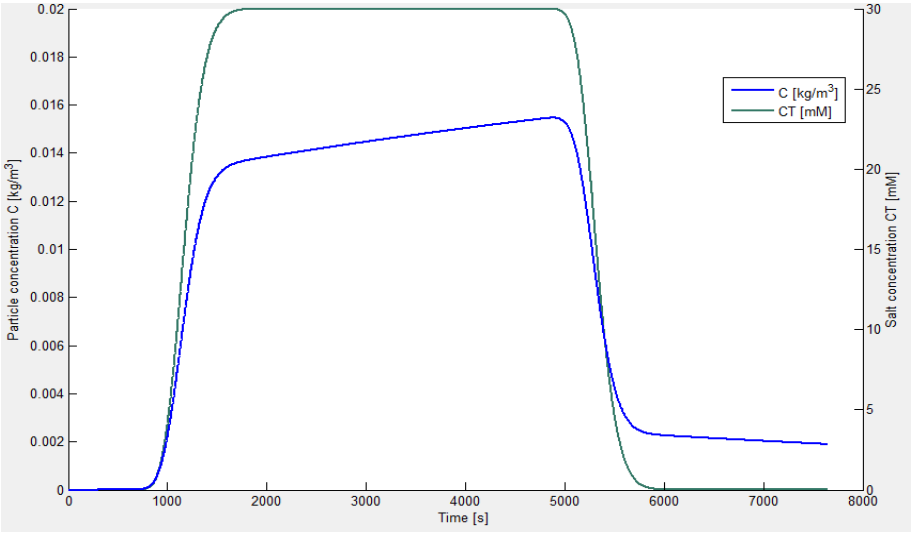

Figure 33. Simulated breakthrough curve for colloid transport in ripening site.

The next graph form the article cited is shown to compare and validate the simulation with MNMs:

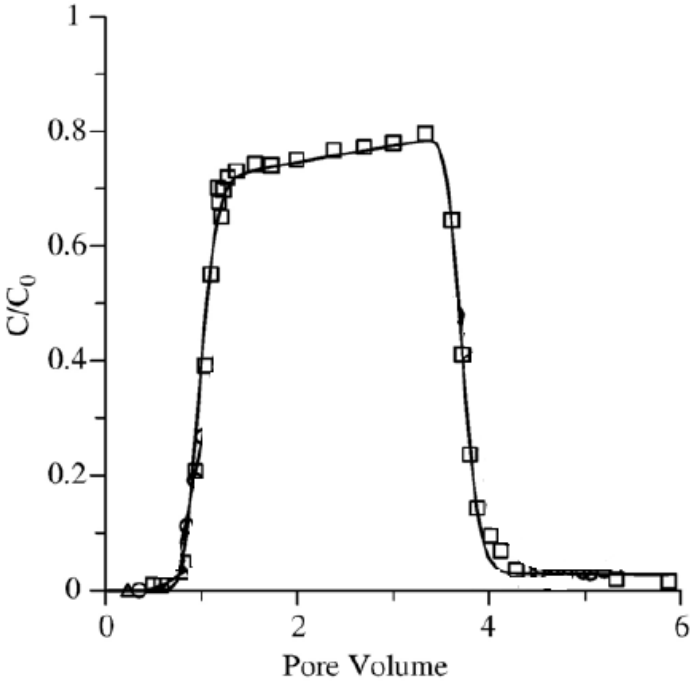

Figure 34. Simulated breakthrough curve for CML colloids in MIX sand, with HYDRUS – 1D code (Source: Torkzaban et al., 2008).

For the MNMs breakthrough curve the highest concentration is 0,0155 kg/m^3 that represents a 77,5% of the input concentration. As happens to the article curve, which reaches the maximum approximately in the 78%.

It is important to remark that the article differential expression is defined in a balance where porosity has been simplified and was necessary to divide the attachment and detachment

coefficients by the porosity. The parameter for the bulk density had been taken as quartz sand an equal to 2650 kg/m^3 and porosity is supposed 0,25 in order to fit the article graph.

Moreover, a NPs decline until C = 0 kg/m^3 is not observed in this case. The injection time for the article graph is 2,7 PV and for the MNMs simulation it has been introduced the equivalent time in seconds. Unfortunately, the data from the article graph is not available so the comparison cannot be numerical. Hence, both charts have the maximum during the same time approximately. The two times where the concentration is the 50% from the total can be interesting in order to compare the breakthrough curves. For the MNMs straining simulation this times are 1274 s from the growth period and 5276 s for the decreasing term. To compare is needed the change to PV using Eq. 12:

$$PV_{50\%\,1} = \frac{1274 \cdot 1{,}62 \cdot 10^{-5}}{0{,}1 \cdot 0{,}25} = 0.83\ PV$$

$$PV_{50\%\,2} = \frac{5276 \cdot 1{,}62 \cdot 10^{-5}}{0{,}1 \cdot 0{,}25} = 3{,}42\ PV$$

Visually comparing with the graph from the article is possible to affirm that those points are approximately coincident. In conclusion, the similarity between both curves validate the linear simulation with MNMs 2018.

The retardation experimental factor can be calculated for this straining simulation in MNMs assuming equilibrium using Eq. 17:

$$R_{exp} = \frac{t_{50}}{t_{50,tracer}} = \frac{1274}{1168} = 1{,}09$$

Below is shown the profile of colloid concentration onto solid phase:

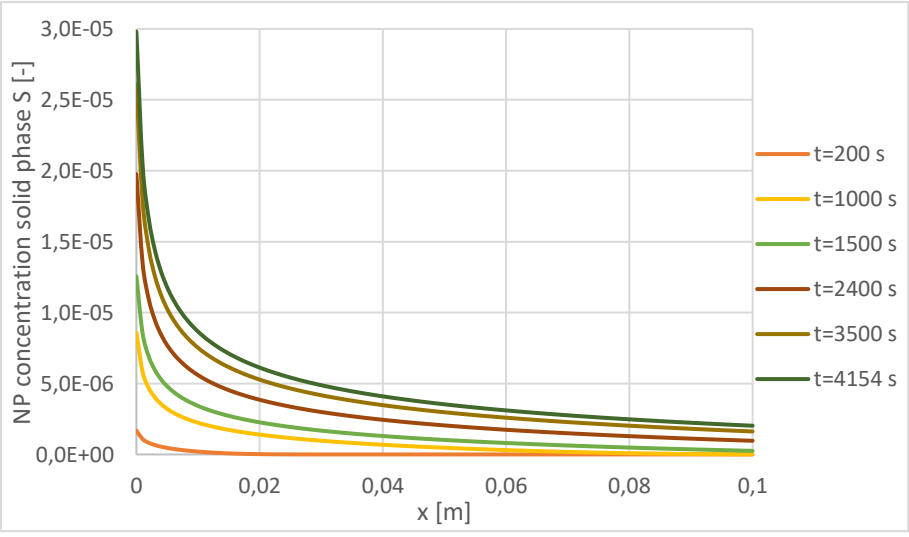

Figure 35. Profile of colloid concentration onto solid phase vs the distance along the column in straining site.

The final concentration in both breakthrough curves (Figure 33 and Figure 34) has this behaviour due to straining mechanism acts at the beginning of the column and needs time to be properly observed. Regarding the hyperbolic profile of colloid concentration onto solid phase showed in the following Figure 35 it could explained the behaviour of the final part in the breakthrough curve. At the end of the injection time, the curves of solid profile are not reaching C = 0 kg/m^3.

Another interesting graph that MNMs 2018 provides is the profile of colloid concentration onto liquid phase:

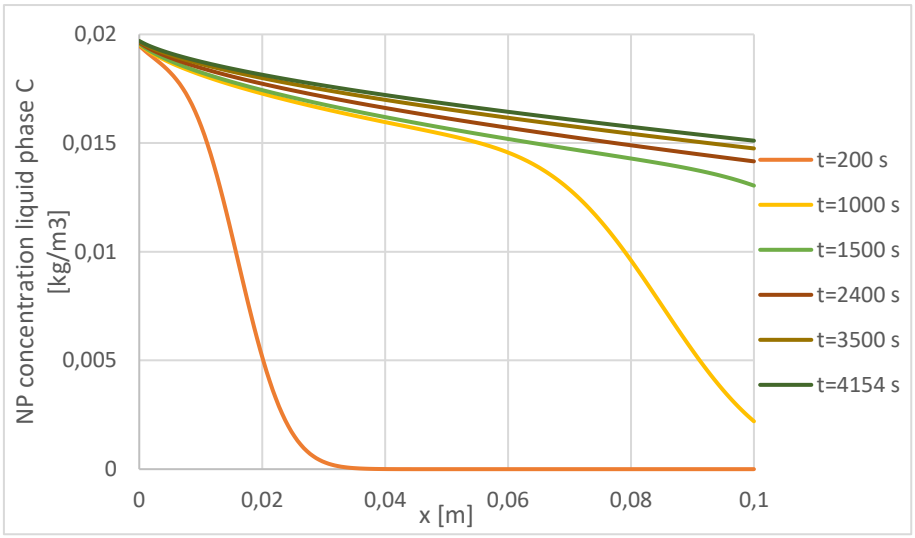

Figure 36. Profile of colloid concentration onto liquid phase vs the distance along the column in straining site.

Finally exporting the data into excel, is possible to create a graph that the program does not include and it is interesting to know if the column deposition of colloids occurs more in the solid or liquid phase. The ordinate axis of this graph is defined as: $C^* = \rho_b \cdot s + c \cdot n$ versus distance:

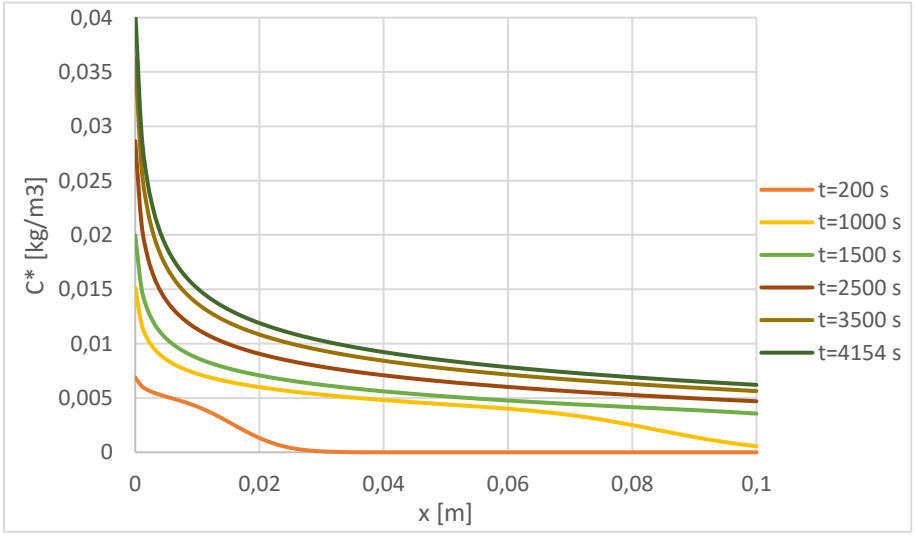

Figure 37. Profile of colloid concentration in solid and liquid phase vs distance along the column in straining site.

Comparing the similarities and differences between the Figure 37 and both concentration profiles provided by MNMs is it possible to conclude wrongly that the concentration in solid phase (S) is mayor in the experiment due the equal shape between Figure 37 and Figure 35. However, to validate in a numerical way it has been calculated a percentage of NPs in liquid phase in four chosen time curves using:

$$Liquid\ phase\ NPs\ [\%] = \frac{n \cdot C}{C^*} \cdot 100$$

The graph obtained is the following:

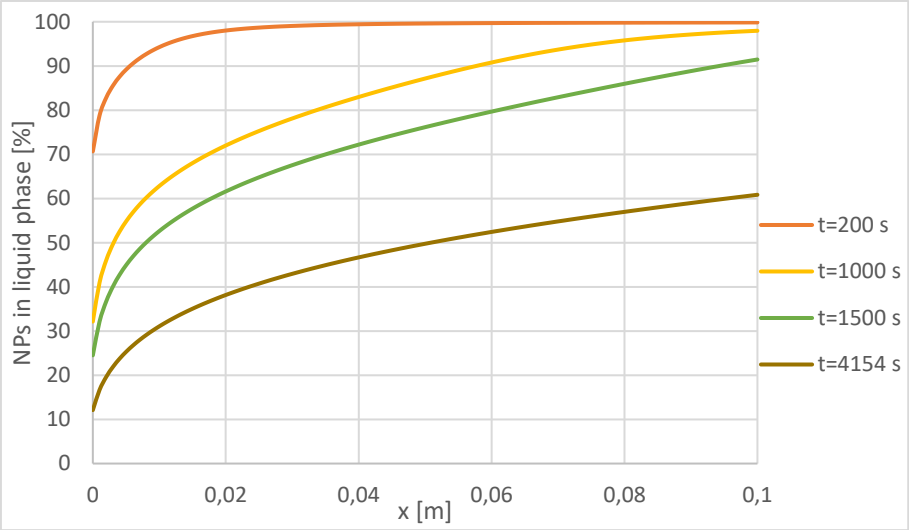

Figure 38. Liquid ratio vs distance along the column in straining site for four chosen times.

The chart depicts that the percentage of NPs in liquid phase is bigger at the beginning of the experiment due to the exceptionally low initial concentration (0,02 kg/m^3).

Moreover, liquid phase percentage is smaller at the beginning of the column for all the chosen times because straining affects the initial part of the column. In addition, it is important to remark that the amount of liquid NPs increases with the distance from the inlet point and decreases in time due to the deposition caused by straining.

5 Modelling a migration test

In this chapter is modelled a migration tests performed in Technical University of Liberec, Czech Republic in 2016 with several nano zero valent iron (nZVI) particles. From all these particles, two of them are compared with the experimental data and one kind of particle has been selected to simulate with MNMs program. This experiment is going to be published very soon.

5.1 Experimental setup

The tests were performed in a column with a length of 2 m and an inner diameter of 20 mm, loaded with standard silica sand. The column was filled as homogeneous as possible using a funnel and afterwards the sand was carefully compacted and positioned vertically between two holders. In order to retard oxidation processes, the column was flushed with nitrogen and saturated with degassed water against the direction of gravity. After saturation and stabilization, several nZVI samples were injected by using a pump at a concentration of 10 g/l and the flow maintained at 100 m/day during the entire test. The water used for the experiment was tap water and the rest of the parameters are summarized in Table 11.

A specifically designed magnetic susceptibility scanner scanned the transport of the iron slurry in the column during injection. The magnetic susceptibility sensor delivered results of distribution and concentration C* of nZVI particles continuously in real time. The column was scanned from 0 to 180 cm every 10 minutes up to minute 90. After 90 minutes of running the experiments, there was an important increase of pressure and experiments stopped (ČERNÍK, 2018).

The following scheme shows the experimental setup for the transport tests of this chapter:

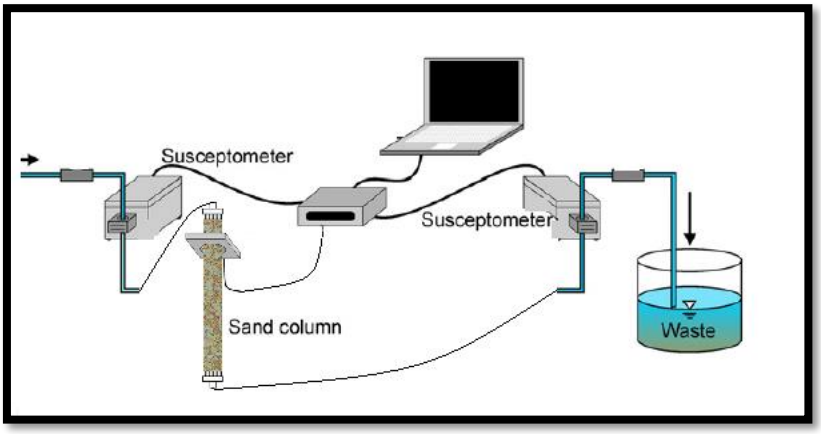

Figure 39. Experimental setup for transport tests (Source: own elaboration).

5.2 Characteristics of the used nanoparticles

Nano zero valent iron (nZVI) particles for groundwater remediation are easy available on the market and supplied mainly in form of an aqueous suspension. This cause a gradual oxidation of the particles and hence a reduction of the content of the active phase (Fe (0)). The main problems of this kind of NPs are the high transport costs (due to the presence of water) and the massive aggregation of NPs, which tends to lead to a poor migration and a decrease of the reactivity with the time (ČERNÍK ET AL., 2016).

To face these problems it has been developed an air-stable technology that has led to the possibility of transporting the NZVI product in the form of a chemically stable powder without any significant loss of the active phase. This technique also reduce the degree of aggregation, help to maximize the migration properties in the aquifer and can be done directly at the site just before the application.

However, there is a less expensive technology: milling or grinding from larger ZVI particles (microscale Fe). The application potential of such a technology is extraordinary because it simultaneously reduces the cost of the application due to the lower cost of the precursor and the preparation technique (ČERNÍK ET AL., 2016).

Most used nZVI include 25P and STAR 197, both obtained from gas reduction of iron oxides by the company NANOIRON s.r.o (Czech Republic). Another kind of ZVI products include A01 iron flakes, obtained by milling in mono-ethylen glycol (MEG) media by the company UVR-FIA GmbH (Germany).

The particle used in this chapter (NA84) and NA64 were obtained at lab scale by top to down approach (milling) in a two-step process of 24 hours each:

- In the first step, Carboryl Iron Powder form BASF (Germany) was milled in a planetary mill (P-5, Fritsch, Germany) at 400 rpm in MEG media. The grinding media used in NA64 sample was 5 mm diameter balls of low carbon steel, while in NA84 the grinding media used was 0,5 mm diameter balls of high carbon steel. In the final part of this step, flakes were obtained (RIBAS ET AL., 2017).
- In the second step, alumina of 5 µm was added (53,6 g/l in the case of NA64 and 80,4 g/l in the case of NA84) in a N_2 atmosphere (ČERNÍK ET AL., 2016).

The following figure shows the SEM images and the granulometry of the NPs tested:

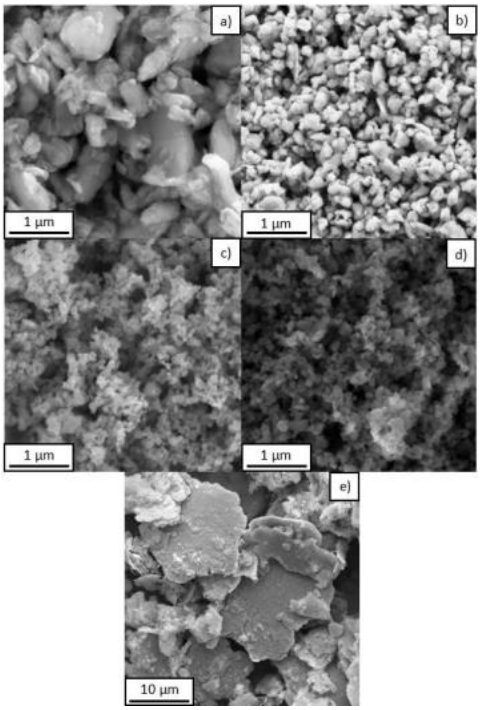

Figure 40. SEM images of the particles: NA64 (a), NA84 (b), 25P (c), STAR 197 (d) and A01 (e) (Source: Ribas, 2017).

The granulometric distribution is shown in Figure 41:

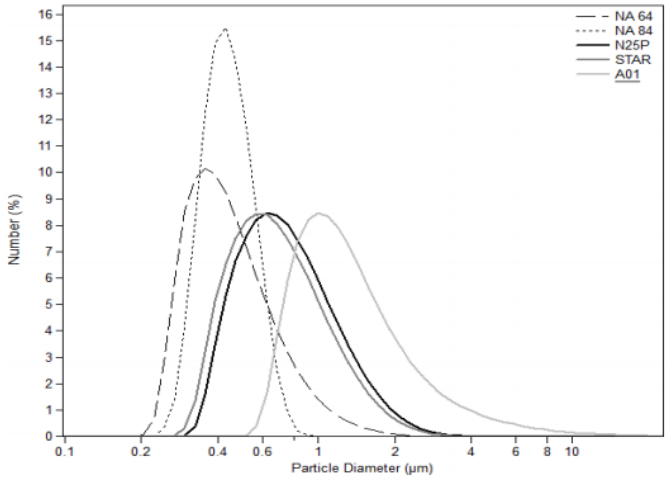

Figure 41. Granulometric distribution obtained by laser diffraction of commercial and used NPs (Source: Ribas, 2017).

According to the ganulometric distribution, the size of the particles range from 200 to 2000 nm in the case of NA64 and from 200 to 1000 nm for NA84. In the case of commercial NPs, SEM values exhibit 110 nm of average for 25P and STAR 197 with maximum values around 330 nm. UVR-FIA A01 NPs showed a mean size around 7350 nm with a maximum of 34170 nm (flake geometry). As it can be seen, the size shown in Figure 41 is higher for 25P and STAR 197 and similar in the case of UVR-FIA A01 flakes. Aggregation due to magnetic effect is a possible explanation of the results shown in granulometry.

Table 9 shows the properties from the nanoparticles of the granulometry profile:

Table 9. Characteristics of the NPs (Source: Ribas, 2017).

Parameter	***NA64***	***NA84***	***25P***	***STAR 197***	***A01***
Fe^0 [%]	78	74	93	78	74
BET [m^2/g]	20,0	29,6	26,1/28,7*	14,6/30*	18
Sedim. Rate [mm/h]	5,64	2,39	-	42-89	1116
Zeta Pot. At pH=8 [mV]	+30	-	-	-30 to -40	-

**Activated.*

The content of ZVI is higher in nanoiron NPs than in the milled particles. The BET area is similar in NA64 and A01, both milled particles, but in the case of NA84 the BET area is similar to nanoiron NPs, probably due to the reduced size of the obtained NPs.

The sedimentation rates of NA64 and NA84 are very low compared with commercial NPs. In the case of A01 the high sedimentation rate could be explained for the high size of particle, but in the case of STAR 197 is difficult to explain from SEM sizes values and can be linked to the agglomeration between particles shown in granulometry figure.

The zeta potential of NA64 and STAR 197 are very good in both cases to guarantee a good stability of the suspension. These zeta potential values have been obtained in suspensions without adding tensoactives. The positive sign of zeta potential in NA64 indicates negative charged particles that could be explained by the presence of alumina. While the negative sign of zeta potential for STAR is typical of iron oxides and the high values indicates that was taking into account only the electrostatic charge, the particles would not agglomerate because repulsion will act. Due to the agglomeration shown in granulometry and the high sedimentation rate measured, magnetism could be an explanation for this behaviour, because from the point of view of zeta potential the electrostatic charges would help with stability.

Another key point to consider is the zeta potential or the charge of the sand. The reference values of zeta potential for the quartz sand are -22,2 to -40 mV (Tosco et al., 2012). This means that sand is positive charged and there will be a repulsive effect with STAR 197 and an attractive effect with NA64 iron.

From all these particles, the NPs NA84 have been chosen for the modelization of mobility in the column with the software MNMs 2018. These particles have the lowest sedimentation rate and did

not shown agglomeration, and hence the stability of the suspensions of these particles is expected without adding any dispersant.

According to the article from ČERNÍK ET AL., 2016, the average size for NA 64 is 470 nm with a maximum particle diameter of 2890 nm. In contrast, the NA 84 has an average particle size of 160 nm with a maximum particle diameter of 540 Nm. Hence, the conclusion to discuss properly the experimental results is that NA64 has a larger size than NA84.

The charge for NA64 has a contrary sign to the one of the sand column (maybe due to alumina rest) this will cause a stronger interaction between particle and the sand. A hypothesis has been done: the charge for NA84 is considered similar to NA64 due to the close characteristic between both NPs.

Comparing the size of these NPs with the case studies simulations performed in the present work, straining effects could be more important as the sand is similar than the simulations but the size is bigger.

5.3 Experimental data

The graphs of this chapter show the results from the migration test experiment in Technical University of Liberec. It has been omitted the first 12 cm (15 data numbers) due to an incomplete scanning from the authors.

The fact that the experimental points begin at the origin of coordinates is that in the migration test the ordinate axis delta frequency is a measure of the magnetic susceptibility (the response of the detector) and the MNMs 2018 program and later excel the y-axis values are particle concentration. Hence, a hypothesis has been done: the assumption that the total magnetic signal is proportional to concentration.

It is important to take into account the length of the column tested. In the current migration test is equal to 2 m and in the previous simulations from articles (linear, blocking, ripening and straining) the range was 0,1 to 0,5 m. The length steps of the experimental data is from 1 cm to 180 cm. In addition, the fitted data are steps and no pulses as the previous case studies references.

This chapter will be focused in the study of the experimental data of two kinds of NPs: the NA64 and the NA84.

The experimentally obtained graph for the nanoparticles NA64 is the following:

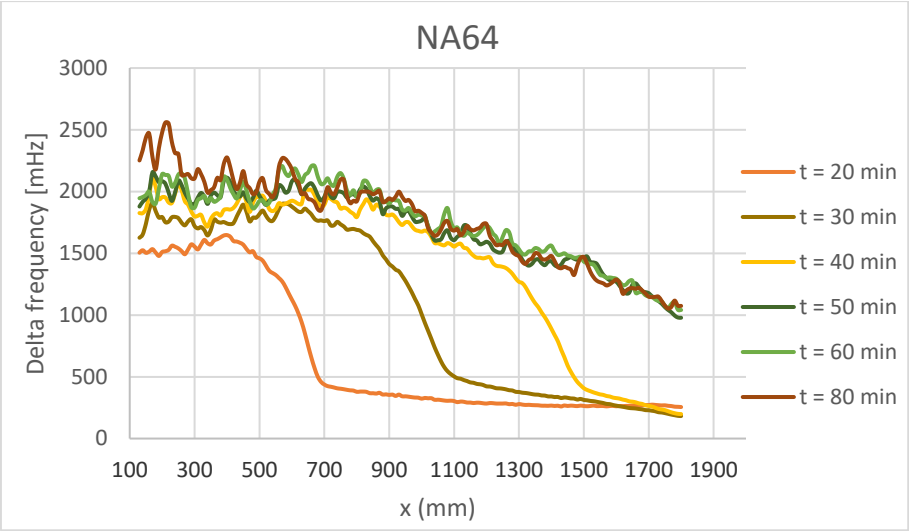

Figure 42. Profile of magnetic susceptibility versus the distance for NA64 particles (Source: Černík, 2018).

Observing the experimental profile for NA64 it is possible to conclude that are not reliable data due to the time curves never reach the C*=0 kg/m^3. This is the reason to rescind this nanoparticles for the simulation with MNMs.

The profile obtained changing only the nanoparticles to NA84 is shown below:

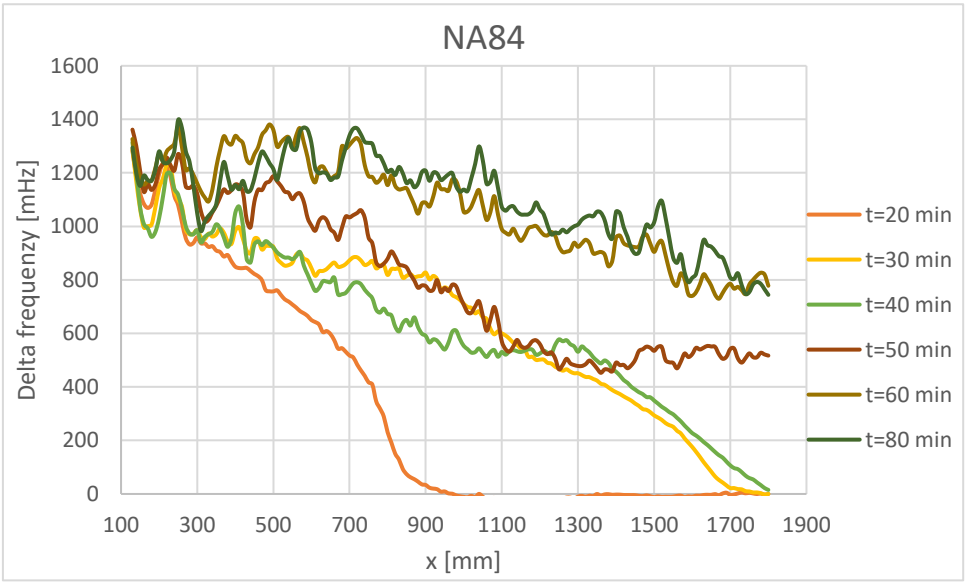

Figure 43. Profile of magnetic susceptibility versus the distance for NA84 particles (Source: Černík, 2018).

It is important to remark the influence of particle bigger size on the mobility (remembering that the sand is the same for both experiments). Considering that NA64 is larger than NA84, the first experiment will have more possibilities of being affected by straining and it will have more gravitational sedimentation and interception between NP and porous media, thus the injection and subsequent remediation will be less efficient. Moreover, larger NPs have less reactivity and this

cause a larger remediation time and costs. It can be observed that the curves "t=30 min" and "t=40 min" for the NA84 particle (Figure 43) are very similar, this behaviour is not typical. In the previous study cases was never observed neither in the bibliography consulted. There is no reference for the close shape for two curves with such a different times. Hence, could be an empirical error caused by the unknown conditions of the experiment.

It is also interesting to pay attention to the first curves for both profiles. In the second case (Figure 43) the "t=20 min", "t=30 min" and "t=40 min" curves enter in the column better than the first case (Figure 42). This observation suggests that NA84 nanoparticles have good mobility in the media, caused by their smallest size and thus less interaction with the porous media (sand).

Nonetheless, to determine in a more detailed way the mechanism that rules the previous experimental data it is necessary to translate the x-axis into time. However, the experiment was carried out measuring the data only once every 10 minutes.

The obtained graph for NA64 particles susceptibility versus time at the outlet of the column is presented below:

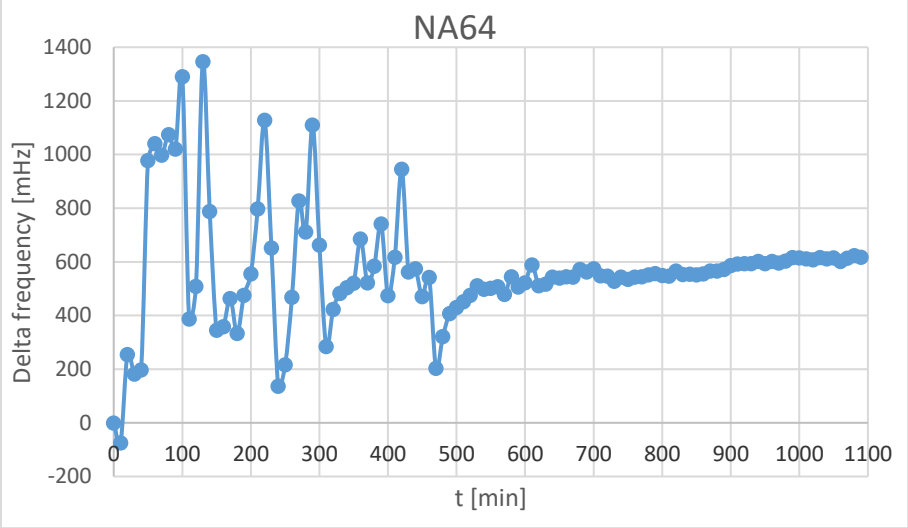

Figure 44. Profile of magnetic susceptibility versus time at the outlet of the column for NA 64 particles.

The available information is scans from 0 to 1090 minutes in steps of 10 minutes. Using Eq. 12 it can be calculated the number of PV for this experiment. It has been taken into consideration t = 1090 min = 65400 seconds and the parameters from Table 11:

$$Number\ of\ PV = \frac{t \cdot Q}{\pi \cdot r^2 \cdot L \cdot n} = \frac{65400 \cdot 1{,}5 \cdot 10^{-7}}{\pi \cdot 0{,}01^2 \cdot 1{,}8 \cdot 0{,}4127} = 42{,}03\ PV$$

For the afterwards simulated NA 84 particles, the graph obtained from the experimental data is:

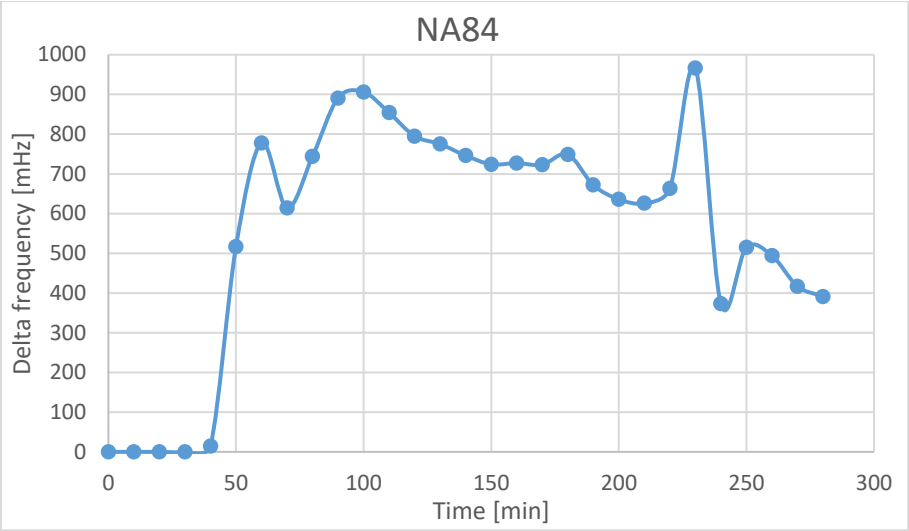

Figure 45. Profile of magnetic susceptibility versus time at the outlet of the column for NA 84 particles.

The available data for NA84 is quite different. There is scans from 0 to 280 min, but in steps of 10 minutes as well. It can be calculated the number of PV (t=16800 s) as previously explained:

$$Number\ of\ PV = \frac{t \cdot Q}{\pi \cdot\ r^2 \cdot L \cdot n} = \frac{16800 \cdot 1{,}5 \cdot 10^{-7}}{\pi \cdot\ 0{,}01^2 \cdot 1{,}8 \cdot 0{,}4127} = 10{,}8\ PV$$

This nanoparticles are chosen to be the simulated ones, for this reason, a further graph needs to be obtained. As it can be observed, after 200 minutes the magnetic susceptibility has interferences and does not follow a logical profile. Hence, it has been taken the decision to omit the afterward times and to suppose the maximum signal of the studied interval as equal to the initial concentration of the experiment C = 10 kg/m^3. The obtained graph with the x-axis in seconds instead of minutes can be seen below:

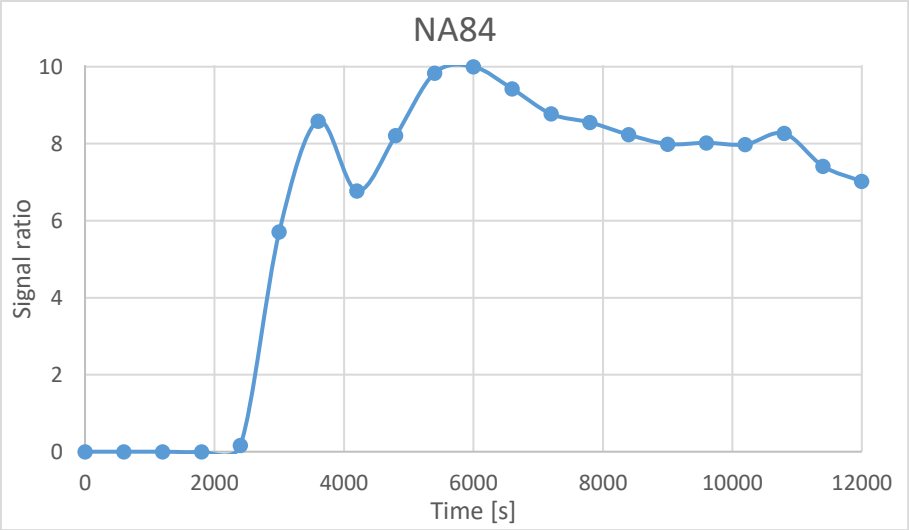

Figure 46. Signal ratio versus time for NA84 particles.

To know the time when time when the concentration is the 50% of the initial one (t_{50}) it is necessary a lineal interpolation from the Figure 45 assuming a linear behaviour between the time points equal to 40 and 60 minutes. The equation used is shown below:

$$y = y_0 + \frac{y_1 - y_0}{x_1 - x_0} \cdot (x - x_0) \qquad \text{Eq. 24}$$

The linear interpolation for this case using the experimental data is:

$$5 = 0{,}17 + \frac{8{,}59 - 0.17}{3600 - 2400} \cdot (t_{50} - 2400)$$

$$t_{50} = 3090\ s$$

It is possible to easily determine the $t_{50,tracer}$. The authors of the experiment report a tracer velocity, from which the time is calculated as shown below:

$$t_{50,tracer} = \frac{L}{v_{tracer}} = \frac{280\ cm}{6{,}94\ cm/min} \cdot \frac{60\ s}{1\ min} = 1555\ s$$

The retardation experimental factor can be calculated for NA84 experimental data assuming equilibrium using Eq. 17

$$R_{exp} = \frac{t_{50}}{t_{50,tracer}} = \frac{3090}{1555} = 1{,}99$$

The sum up of the retardation factors obtained during this project is a useful value to help identifying the main mechanism:

Table 10. Retardation factor for all the case studies.

	Linear	***Blocking***	***Ripening***	***Straining***
R_{exp}	2,73	1	1,3	1,09

Finally, rejecting the linear mechanism for the simplicity and low probability to rule experimental data, the retardation factor values indicate that ripening is the mechanism that will fit better the retard of the breakthrough curve, as happens in the following subchapters.

The Figure 46 is imported to MNMs program and used as a reference to fit the breakthrough curve and modelling the experiment.

5.4 Modelling NA84 with MNMs

In this chapter, it has been carried out two simulations for NA84 nanoparticles. The ionic strength is constant like the previous simulations and it has been taken as value equal to 10 mM.

It is important to remark that the porous media clogging is not considered due to the lack of data and information from the experiment authors. Hence, an assumption has been done: this phenomenon is enough little and reversible to not be considered in the MNMs simulation.

It has been taken into consideration one active site for each simulation due to the software does not allow to export a two-site modelling to Excel and therefore, the total concentration graph C* cannot be created and compared with the experimental data previously presented in Figure 43. The first simulation assumes the ripening active site and the second the straining.

A maximum injection time has been defined equal to 13800 seconds to observe the behavior after a prolonged time. The parameters already explained and the ones provided by the author of the experiment can be seen below:

Table 11. Properties for the simulation of the experiment for NA84 (Source: Černík, 2018).

Parameter	***Parameter explanation***	***NA64***	***NA84***	***Units***
L	Column length	1,8		m
r	Radius of the column	0,01		m
Q	Discharge rate	$1{,}5 \cdot 10^{-7}$		m^3/s
α_L	Dispersivity	$1 \cdot 10^{-3}$		m
n	Clean Bed effective porosity	0,4127		-
ρ_b	Density of the sand grains	2650		kg/m^3
d_{50}	Mean diameter of sand grains	$1{,}2 \cdot 10^{-3}$		m
IS	Ionic Strength	10		mM
$t_{inj\ maxim}$	Injection maxim time	13800		s
C_{in}	Injection concentration	10		g/l
C_0	Initial concentration	0		g/l

The values for dispersivity and mean diameter of sand grains are assumed based on the references and the previous study cases included in this work. Further, the porosity is considered constant.

To achieve a good fitting it has been carried out 4 simulations for the ripening active site and 4 for straining as summarized in the tables below.

The fist table define the specific parameters for the different options with the ripening active site:

Table 12. Properties for the ripening site for NA84.

Parameter	***A rip***	***B rip***	***C rip***	***D rip***
k_{att} [s^{-1}]	$2{,}6 \cdot 10^{-2}$	$2{,}6 \cdot 10^{-2}$	$3 \cdot 10^{-2}$	$3 \cdot 10^{-2}$
k_{det} [s^{-1}]	$4 \cdot 10^{-2}$	$3 \cdot 10^{-2}$	$4 \cdot 10^{-2}$	$3{,}9 \cdot 10^{-2}$
A_{rip}	3000	3000	4000	3500
β_{rip}	1,7	1,7	1,5	1,6

The specific chosen parameters for the straining simulations options in MNMs are:

Table 13. Properties for the ripening site for NA84.

Parameter	***A str***	***B str***	***C str***	***D str***
k_{att} [s^{-1}]	$2 \cdot 10^{-2}$	$5 \cdot 10^{-2}$	$2 \cdot 10^{-2}$	$5 \cdot 10^{-2}$
k_{det} [s^{-1}]	$2 \cdot 10^{-3}$	$1 \cdot 10^{-2}$	$5 \cdot 10^{-3}$	$3 \cdot 10^{-3}$
β_{str}	0,432	0,432	0,432	0,432

The stress periods time chosen (no matter the active site) are the following:

Table 14. Stress period time for NA84 simulation.

Stress Period	**1**	**2**	**3**	**4**	**5**	**6**	**7**
Δt [s]	1200	600	600	600	600	1200	9000
Time [s]	1200	1800	2400	3000	3600	4800	13800

Once all the parameters are introduced in the MNMs program and the simulations carried out, the C* graph is created for each one and selected the best option for each site. The results are showed in the subsequent chapters.

5.4.1 Ripening simulations

For the ripening site, after the simulation of all the options, “C rip” is the one that fits better the experimental data. The breakthrough curve that the MNMs software provides is shown with the blue line, the tracer in green and the experimental data imported in black:

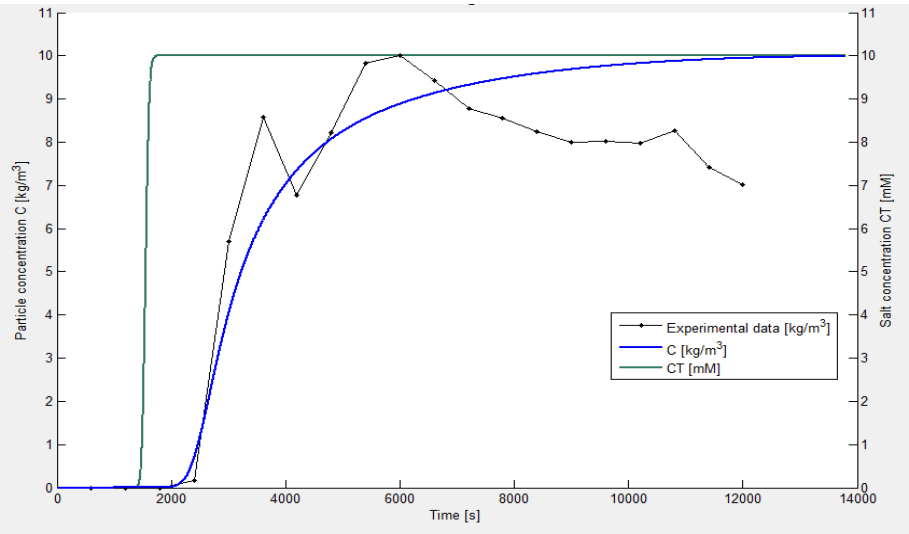

Figure 47. Simulated breakthrough curve for NA84 in ripening site.

It experimental and simulates curves have a similar silhouette and a coincident growing up time, due to the nearer retardation factor value compared with straining (as shown in Table 10). The main difference is that there is no decline for simulation data, in contrast to the experimental.

Below is shown the profile of colloid concentration onto solid phase:

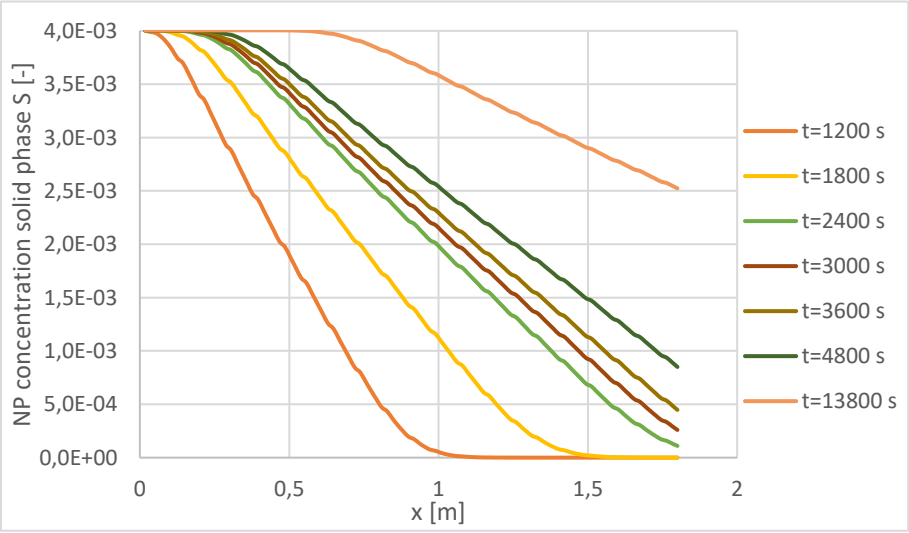

Figure 48. Profile of colloid concentration onto solid phase vs the distance along the column in ripening site for NA84.

Another interesting graph that MNMs 2018 provides is the profile of colloid concentration onto liquid phase:

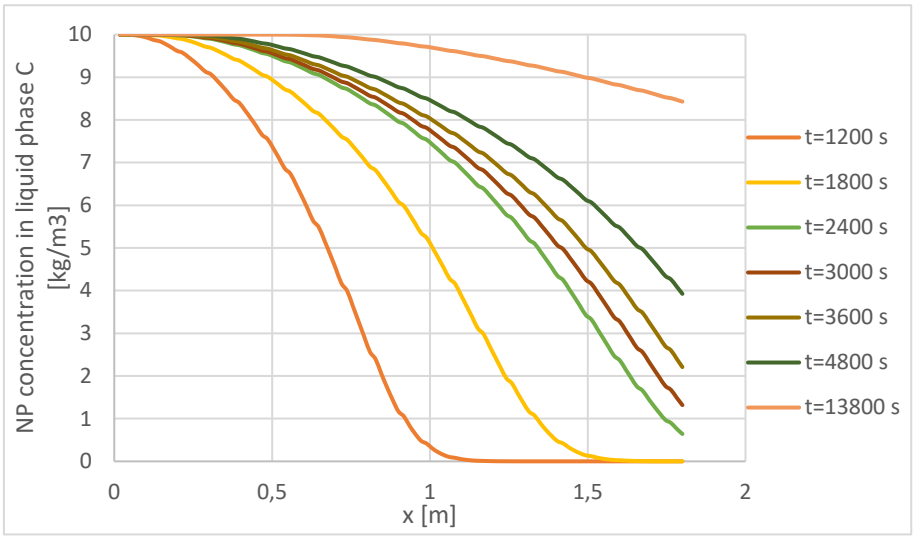

Figure 49. Profile of colloid concentration onto liquid phase vs the distance along the column in ripening site for NA84.

Finally exporting the data into excel, is possible to create a graph that the program does not include and it is the one that will be compared with the experimental data (Figure 43) to validate and compare the simulation. The ordinate axis of this graph is defined in Eq. 21 as: $C^* = \rho_b \cdot s + c \cdot n$ and the abscissa axis is the distance along the column in meters.

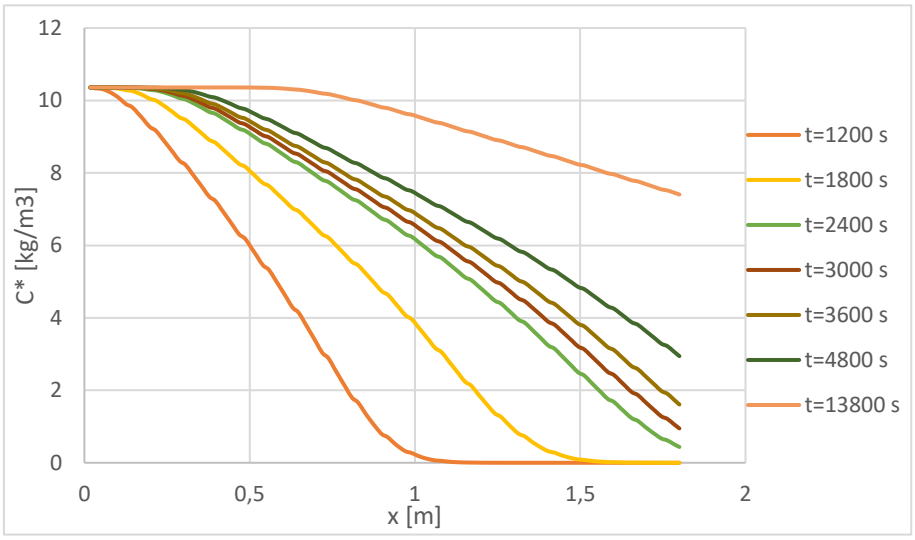

Figure 50. Profile of colloid concentration in solid and liquid phase vs distance along the column in ripening site for NA84.

The similarities between this last total concentration profile and Figure 43 are the approximate time when the "t=1200 s" reaches the C*=0 kg/m^3, for both is around 0,9 meters. Moreover, the three first time curves end in almost the zero total concentration in the simulation and it happens the same in the experimental curves. The choice of ripening active site is justified due to the different

sign of the charges of the sand and the NA84 particle. Ripening is the process of granular media conditioning during which clean media captures particles and becomes more efficient at capturing additional particles, the positive charge for the sand used in the experiment and the negative of NA84 particles can be the reason why this mechanism is the predominant one.

5.4.2 Straining simulations

For the straining site, the option "B str" is the one that fits better the experimental data. The breakthrough curve that the MNMs software provides is shown with the blue line, the tracer in green and the experimental data imported in black:

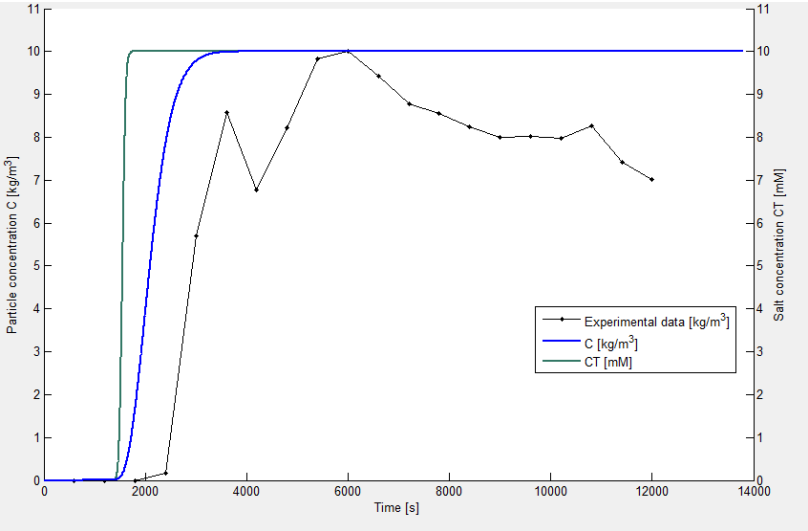

Figure 51. Simulated breakthrough curve for NA84 in straining site.

There is a difference between the experimental growing up time and the theoretical, in straining this retard cannot be represented as well as with ripening.

Moreover, the breakthrough curve silhouette for ripening site fits visually better the experimental data than the straining profile, however it is important to remark that experimental data is not concentration data but a magnetic signal and that has been adapted to a made-up scale. Therefore, is better to compare the C* graph, because the experimental breakthrough curve has one value each 10 minutes. Below is shown the profile of colloid concentration onto solid phase:

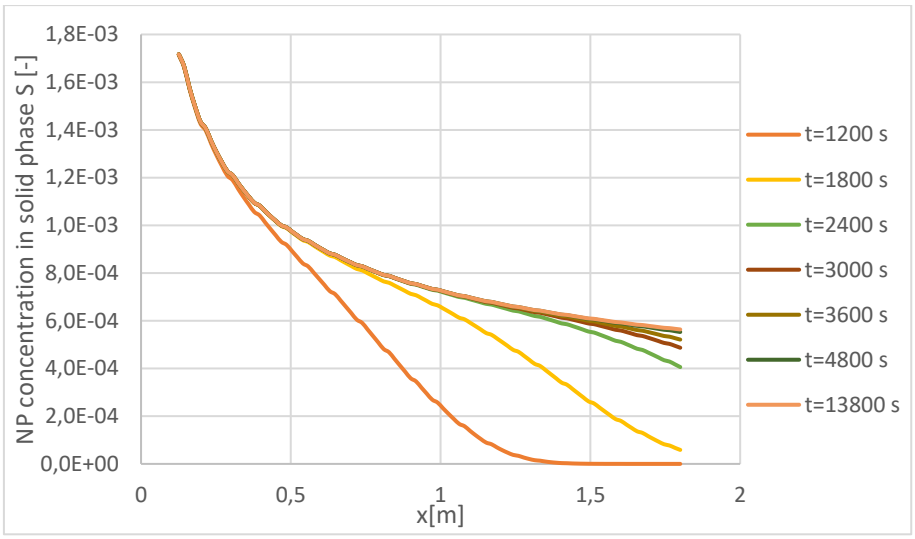

Figure 52. Profile of colloid concentration onto solid phase vs the distance along the column in straining site for NA84.

The last graph that MNMs 2018 provides is the profile of colloid concentration onto liquid phase:

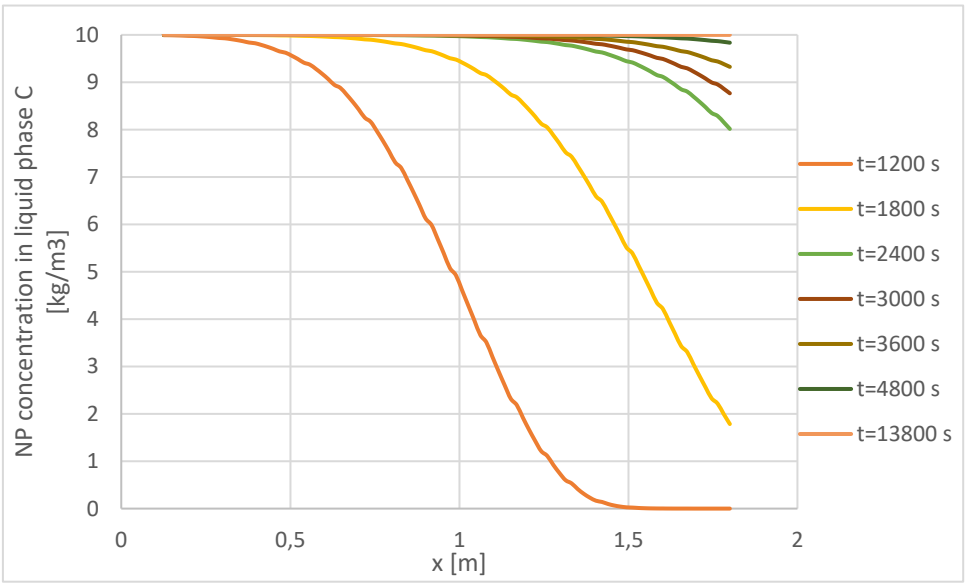

Figure 53. Profile of colloid concentration onto liquid phase vs the distance along the column in straining site for NA84.

Finally exporting the data into excel, is possible to create a graph that the program does not include and it is the one that will be compared with the experimental data (Figure 43) to validate and compare the simulation. The ordinate axis of this graph is defined in Eq. 21 as: $C^* = \rho_b \cdot s + c \cdot n$ and the abscissa axis is the distance along the column in meters.

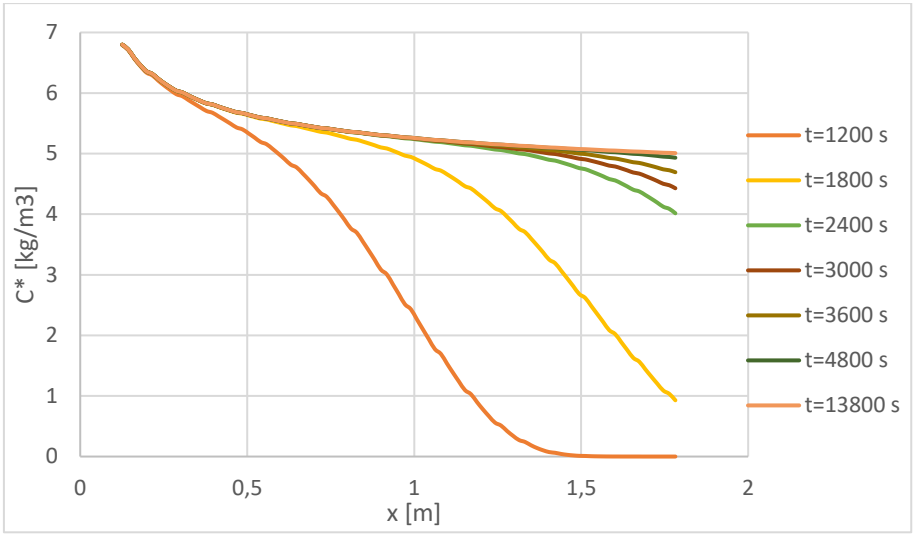

Figure 54. Profile of colloid concentration in solid and liquid phase vs distance along the column in straining site for NA84.

Observing the experimental graph of magnetic susceptibility versus distance along the column it can be easily recognize a staining mechanism for the decrease of curves even for elevated times, and happens the same for the C* from the MNMs simulation.

Comparing the total concentration profile with the experimental Figure 43 can be stated that the first time curve does not fit the time when reaching C*=0 kg m^3 as well as ripening. Even though, straining is the theoretically more adequate mechanism to explain the experiment due to it occurs when colloids are retained in pores that are smaller than some critical size and bigger particle as the used in the migration test favour this phenomenon.

Moreover, modelling with straining is more reliable than ripening due to there is only two degrees of freedom (k_{att} and k_{det}), considering β_{str} constant for all the possible simulations.

6 Environmental impact

As this work was completely developed digitally, an environmental project impact cannot be done. Nevertheless, as the project is focused on the study of the mobility of NPs in porous media it will help to study also its environmental impact. Safety and environmental impact are always very important factors to consider. However, in the present project, where an environmentally friendly use of nanotechnology is studied, they become exceptionally important.

Little work to date has been undertaken on assessing the sustainability of NPs used in remediation, although some NGOs have raised questions about the sustainability of nanomaterial production (e.g., Friends of the Earth, 2010), particularly its energy budget (BARDOS ET AL., 2015).

Uncertainties about the environmental impact of the use of reactive NPs to ecosystems is identified as a key factor to the restricted use of them in soil and groundwater remediation.

Decreasing particle size and increasing reactivity are properties that may render a substance more toxic. Thus, the very properties that make nanoparticles technologically interesting may place them in a novel category of potentially toxic substances. A number of studies exist concerning the toxicity of nanoparticles. Generally, these studies suggest that smaller particles are more toxic than larger ones, although large differences among different particle types exist (OBERDÖRSTER ET AL., 2009).

In addition, it was pointed out that toxicological and ecotoxicological methods are not sufficient to deal with the problems that may arise in nanoparticles (Scientific Committee on Emerging and Newly Identified Health Risks - SCENIHR, 2006). About the procedures that the SCENIHR recommends to take with the nanoparticles regarding their solubility and persistence: in the nanoparticles of high solubility, the procedure to be followed is that which is taken with the macroscopic material. If the persistence is low and the nanoparticle tends to degrade, the behaviour and toxicity of the degraded products must be taken into account. On the other hand, if the solubility is low as well as its tendency to degrade, the nanoparticles can accumulate in the organism and interfere in its correct functioning (Scientific Committee on Emerging and Newly Identified Health Risks - SCENIHR, 2006).

It has been proved that NPs reactivity and toxicity change with time. It is believed that as NPs interact within the soil matrices they become less reactive and therefore less toxic with the time. As chemical contaminants age in the soil, their reactivity is reduced along with their bioavailability and toxicity (RODRIGUES, 2016). Also appropriate measures should be in place relating to the manufacture and transport of NPs, so occupational exposure scenarios are minimized (BARDOS ET AL., 2015).

7 Conclusions

This project contributes to a better understanding of fundamental processes and important parameters governing nanoparticles transport and retention. After the analysis and discussion of the case studies simulations and real migration test modelling carried out in the current project, it is claimed to have increased the knowledge about the topic.

It has been studied the mobility of NPs in a paramount field to understand the behaviour of colloidal suspensions in groundwater, either as a contaminant or an engineered solution to remediate a polluted aquifer.

Understanding the functioning of the interactions between particle and porous media allows considering and modelling linear, blocking, ripening and straining mechanisms with few fitting parameters. The four first case studies (with different parameters from the articles cited in each chapter) have been validated, showing a very good matching with the published simulations. This important part of the project allows identifying easily the patterns of concentration of NPs in solutions and on the porous media, in space and time. The knowledge obtained will be used in the afterwards modelling of a real migration test, using the same software for the entire project.

The migration test is a new unpublished experiment and it has been evaluated for modelling. Patterns previously identified point to ripening or straining as key mechanisms. The software does not allow to export a two-site modelling to Excel. Hence, both mechanisms have been separately simulated for one selected nanoparticle, the NA84, with the difficult to fit the results to one single simulation. The active sites chosen are ripening and straining, however, it is not possible to conclude which one fits better. Both are discussed and justified in the corresponding chapter.

In the process of choosing the most suitable operating parameters (not provided by the experiment owner) to achieve the best modelling possible, it was necessary to simulate several cases to determine the most similar one. The objective to fit several profiles at the same time is ambitious; very few references face this situation.

Finally, it is considered very interesting to be able to carry out simulations with non-constant ionic strength in the future. In addition, as proposal for enlargement, applying the knowledge obtained in this end-of-degree project to carry out three-dimensional simulations would be alluring in order to get closer to a more realistic configuration.

8 Economic analysis

8.1 Time programming

The porpoise of the current subchapter is to provide a general view of the programming time for the project. It was needed a Gantt chart to illustrates the schedule followed during this end-of-degree thesis. On the vertical axis is listed the main tasks that were realized and time intervals dedicated for each assignment on the horizontal axis.

The following figure shows the Gantt diagram followed from September to the date of delivery:

	Task name	Start day	Finish date	2017				2018				
				sep	oct	nov	dic	ene	feb	mar	abr	may
1	Selection of the project topic	03/09/17	08/09/17									
2	Definition of the objectives and scope	18/09/17	25/09/17									
3	Reviewing of the literature	04/10/17	26/11/17									
4	Familiarization with the software MNMs	12/11/17	12/01/18									
5	Writting a first draft report	26/12/17	09/02/18									
6	Extended literature reviewing	05/01/18	15/02/18									
7	Simulating the 4 article cases	15/02/18	27/03/18									
8	Modelling and simualting a migration test	30/03/18	15/05/18									
9	Writting the final report	15/05/18	01/05/18									

Figure 55. Gantt diagram for the present project.

8.2 Costs of the project

The present section consists of the analysis of the economic aspects related to this end-of-degree thesis. In order to evaluate the total costs derived from the development of this project, the costs that are listed below have been taken into account:

- Software
- Material
- Personnel

8.2.1 Software resources

First, the software licences costs are shown in the table below:

Table 15. Software costs.

Software	***Price [€]***
Microsoft Office Professional 2016	539
Annual license MatLab R2018a	800
Software total costs	**1.339**

Regarding Microsoft Office®, the cost has been extracted from the official Microsoft Store. With respect to MatLab®, it has been considered that an annual license was enough for this project and has been obtained from the official MathWorks web page.

The license for the program MNMs 2018 is free for academic usage like this project, so no more software costs are added.

8.2.2 Material resources

The material resources costs take into account the physical elements that has been used. In this project:

Table 16. Material costs.

Material	***Price [€]***
Computer, mouse and keyword	700
Office material (scan, paper, calculator)	50
Material total costs	**750**

8.2.3 Personnel costs

It has been considered that an engineer with no working experience developed this project. Eight month were dedicated on the project from September 2017 to April 2018 according to Gantt diagram. The hours were on part time, combined with a full time job. Hence, the time dedicated each week are 4 hours, 5 days.

$$Personnel\ costs\ \left[\frac{€}{8\ months}\right] = \frac{4\ hours}{1\ day} \cdot \frac{30\ days}{1\ month} \cdot 8\ months = 960\ h$$

Fixing the price per work hour as 15€ and considering the same price for all the tasks represented in the Gantt diagram (Figure 55), the cost of engineering sums to **9.600€**.

To sum up, the following table shows the budget for the direct costs:

Table 17. Total direct costs.

Concept	***Price [€]***
Software	1.339
Material	750
Personnel	9.600
Direct costs	**11.689**

8.2.4 Total budget

This chapter is a sum up of the previous ones with the addition of the indirect costs (printing, electricity…) with a hypothetical value of the 5% the direct costs. In addition, it has been taken into consideration the VAT (value-added tax, or IVA in Catalan), equal to the 21% of the sum of direct and indirect costs.

The next table describes the total cost of the project:

Table 18. Total cost for the project.

Concept	***Price [€]***
Direct costs	11.689
Indirect costs	584,45
Total project cost	**12.273,45**
TOTAL COST + IVA	**14.850,87**

The total costs of this project is **14.850,73 €.**

9 References

Bianco, C., Patiño Higuita, J. E., Tosco, T., Tiraferri, A. and Sethi R. Controlled deposition of particles in porous media for effective aquifer nanoremediation. *Scientific Reports* **2017**, *7* , 12992.

Binnie, C. and Kimber, M. *Basic water treatment*, 4th ed.; Thomas Telford: London, England, 2009; pp. 141 – 146, 978-0-7277-3608-6.

Bradford, S. A. and Bettahar, M. Concentration dependent transport of colloids in saturated porous media. *Journal of Contaminent Hydrology* **2006**, *82*, 99 -117.

Bradford, S.A., Simunek, J., Bettahar, M., Van Genuchten, M., and Yates, S. R. Modelling colloid attachment, straining and exclusion in saturated porous media. *Environmental Science Technology* **2003**, *37*, 2242 – 2250.

Bradford, S. A., Simunek, J., Bettahar, M., Van Genuchten, M. T. and Yates, S. R. Significance of straining in colloid deposition: evidence and implications. *Water Resources Research* **2006**, *42*, W12S15.

Bradford, S. A., Yates, S. R., Bettahar, M., and Simunek J. Physical factors affecting the transport and fate of colloids in saturated porous media. *Water Resources Research* **2002**, *38(12),* 1327-1339.

Bravaccini, G. Estudio de la movilidad de nanopartículas en hierro y óxidos de hierro aplicadas a la remediación del agua subterránea. Final degree project, Universitat Politècnica de Catalunya, Barcelona, Spain, 20-9-**2017**.

Černík, M., Pešková, K., Filip, J., Marti, V. and Auffan, M. DL 2.2: Assessment of nanoparticles performance for the removal of contaminants – nZVI particles. *NanoRem FP 7 Project No 309517* **2016**. Available online: www.nanorem.eu (accessed on 22-03-2018).

Černík, M. (Technical University of Liberec, Liberec, Czech Republic). Personal communication, February **2018**.

EPA (U.S. Environmental Protection Agency). Pump-and-treat groundwater remediation, a guide for decisions makers and practitioners. *EPA/625/R-95/005. Office of research and development* **1996**, Washington DC.

EPA (U.S. Environmental Protection Agency). A citizen's guide to pump and treat. *EPA/542-F-12-017. Office of solid waste and emergency response* **2012**, Washington DC.

Hosseini, S. M. and Tosco, T. Transport and retention of high concentrated nano – Fe/Cu particles through highly flow-rated packed sand column. *Water research* **2013**, *47*, 326 – 338.

Karn, B., Kuiken, T. and Otto, M. Nanotechnology and in situ remediation: a review of the benefits and potential risks. *Environ Health Prospect* **2009***, 117*, 1823 – 1831.

Kretzschmar, R., Borkovec, M., Grolimund, D. and Elimelech, M. Mobile subsurface colloids and their role in contaminant transport. *Advances in Agronomy* **1999**, *66*, 121 – 193.

Logan, B. E, Jewett, D. G., Arnold, R. G., Bouwer, E. J. and O'Melia, C. R. Clarification of clean-bed filtration models. *Journal of Environmental Engineering* **1995**, *121*, 869 – 873.

McDowell, L. M., Hunt, J. R. and Sitar, N. Particle transport through porous media. *Water Resources Research* **1986**, *22*, 1901 – 1921.

Messina, F., Marchisio, D. L., Sethi, R. An extended and total flux normalized correlation equation for predicting single-collector efficiency. *Journal of colloid and interface science* **2015**, *446*, 185 – 193.

Mueller, N. C., Braun, J., Bruns, J., Černík, M., Rissing, P., Rickerby, D. and Nowack, B. Application of nanoscale zero valent iron for groundwater remediation in Europe. *Environmental science and pollution research* **2012***, 19*, 550 – 558.

Mueller, N. C. and Nowack, B. Nanoparticles for remediation: solving big problems with little particles. *Elements* **2010***, 6 (6)*, 395 – 400.

NanoRem CL:AIRE NanoRem Bulletin nº 6. Forecasting nanoparticle transport in support of in situ groundwater remediation **2017**. Available online: https://www.claire.co.uk/nanorem (accessed on 18-01-2018).

Oberdörster, G., Stone, V. and Donaldson, K. Toxicology of nanoparticles: a historical perspective. *Nanotechnology* **2009***, 1 (1)*, 2 – 25.

OST-founded technologies. Available online: http://infohouse.p2ric.org/ref/14/13983.htm (accessed on 15-04-2018).

Ribas, D. In situ groundwater remediation treatments: natural denitrification study and nano Zero Valent Iron production. Ph. D. thesis, Universitat Politècnica de Catalunya, Manresa, Spain, 23-01-**2017**.

Pawari, M. J. and Gawande, S. Ground water pollution and its consequences. *International journal of engineering research and general science* **2015***, 3 (4)*, 773 – 776.

Torkzaban, S., Bradford, S. A., Van Genuchten, M. T. and Walker, S. L. Colloid transport in unsaturated porous media: the role of water and ionic strength on particle straining. *Journal of Contaminant Hydrology* **2008**, *96*, 113 – 127.

Tosco, T., Bianco, C. and Sethi, R. MNMs 2015 Micro- and nanoparticles transport, filtration and clogging model – suite. A comprehensive tool for design and interpretation of colloidal particle transport in 1D Cartesian and 1D radial systems. *Polytechnic University of Torino* **2015**, *24*, 10129 (Torino, Italy).

Tosco, T., Bianco, C. and Sethi, R. A 3-dimensional micro- and nanoparticle transport and filtration model (MNM3D) applied to the migration of carbon-based nanomaterials in porous media. *Journal of Contaminant Hydrology* **2016a**, *193*, 10-20.

Tosco, T., Bianco, C. and Sethi, R. Taking Nanothechnological remediation processes from Lab scale to end user applications for the restoration of a clean environment. *NanoRem* **2016b**, *project Nr. 309517*. EU, 7th FP, NMP.2012.1.2.

Tosco, T., Bosch, J., Meckenstock, R. U. and Sethi, R. Transport of ferrihydrite nanoparticles in saturated porous media: role of ionic strength and flow rate. *Environmental Science and Technology* **2012**, *46 (7),* 4008-4015.

Tosco, T., Papini, M.P., Viggi, C.C., Sethi, R. Nanoscale zerovalent iron particles for groundwater remediation: a review. *Journal of Cleaner Production* **2014**, *77*, 10 – 21.

Tosco, T. and Sethi, R. MNM1D – Micro- and nanoparticle transport model in saturated porous media. Numerical solution of colloid transport in 1D systems. *Polytechnic University of Torino* **2008**, *24*, 10129 (Torino, Italy).

Tosco, T. and Sethi, R. MNM1D: A numerical code for colloid transport in porous media: Implementation and validation. *American Journal of Environmental Sciences* **2009,** *5 (4),* 517 – 525.

Tosco, T., Tiraferri, A. and Sethi, R. Ionic Strength dependent transport of microparticles in saturated porous media: modelling mobilization and immobilization phenomena under transient chemical conditions. *Environmental Science and Technology* **2009**, *43 (12),* 4425 – 4431.

Tratnyek, P.G. and Johnson, R.L. Nanotechnologies for environmental cleanup*. Nano Today* **2006***, 1*, 44 – 48.

Van Genuchten, M. Th., Šimunek, J., Leij, F. J., Toride, N. and Šejna M. STANMOD: Model Use, Calibration, and Validation*. Transactions of the ASABE* **2012**, *55(4),* 1353 – 1366.

Wang, C., Bobba, A. D., Attinti, R., Shen, C., Lazouskaya, V., Wang, L. and Jin, Y. Retention and transport of silica nanoparticles in saturated porous media: effect of concentration and particle size*. Environmental Science and Technology* **2012**, *46,* 7151 – 7158.

Yao, K., Habibian, M., and O'Melia, C. Water and wastewater filtration: concepts and applications. *Environmental Science and Technology* **1971***, 5(11),* 1105 – 1112.